Ceramics International 51 (2025) 58481–58500

Contents lists available at ScienceDirect

Ceramics International

journal homepage: www.elsevier.com/locate/ceramint

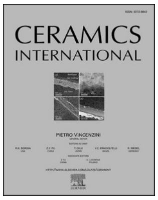

Relation between interfacial adhesion and hardness of electrode materials in electrolyte supported solid oxide cells

Borhan Uddin Manam [a,*], Nico Langhof [a], Carolin Sitzmann [a,d], Stefan Schafföner [a,b,c]

[a] *University of Bayreuth, Chair of Ceramic Materials Engineering, Prof.-Rüdiger-Bormann-Str.1, 95447, Bayreuth, Germany*
[b] *Bayreuth Center for Materials Science and Engineering, Prof.-Rüdiger-Bormann-Str.1, 95447, Bayreuth, Germany*
[c] *Bavarian Polymer Institute, Universitätsstraße 30, 95447, Bayreuth, Germany*
[d] *Fraunhofer ISC, Center for High Temperature Materials and Design HTL, Gottlieb-Keim-Straße 62, 95448, Bayreuth, Germany*

ARTICLE INFO

Handling Editor: Dr P. Vincenzini

Keywords:
Solid oxide cells
Barrier layer
Interfacial adhesion
Micro-indentation

ABSTRACT

Solid oxide cells (SOCs) need to be robust to withstand high thermo-mechanical stress inside the stacks at temperatures longer than 800 °C during operation. To determine this robustness of SOCs, it is necessary to investigate key mechanical properties of the electrolyte and electrodes as well as the interfacial adhesion within the membrane electrode assembly (MEA). Without adequate adhesion between the electrolyte and the electrodes, the cell performance might degrade, leading to reduced stack performance. In the present study, the key mechanical properties such as hardness and elastic modulus of the gadolinium doped ceria oxide (GDC) barrier layer along with the nickel oxide (NiO) and GDC based fuel electrode (NiO/GDC) as well as the air electrode composed of lanthanum strontium cobalt ferrite (LSCF) and GDC (LSCF/GDC) were determined by means of micro-indentation tests. Subsequently, the interfacial adhesion strength between the GDC barrier layer and the 3 mol % yttria stabilized zirconia (3YSZ) electrolyte as well as the interfacial adhesion strengths between the electrode composites and the 3YSZ electrolyte in ultrathin SOCs (140–150 μm) were evaluated by scratch tests. It was observed that the GDC barrier layer had ~80 % higher interfacial adhesion strength with the 3YSZ electrolyte than the electrode composites. Additionally, a relation was found that with the increase of hardness of the electrode materials, the interfacial adhesion between the electrode materials and electrolyte increases. The obtained results might contribute to the further optimization of the manufacturing process and long-term operations of SOCs.

1. Introduction

Solid oxide cells (SOCs) are one of the most promising technologies for highly efficient sustainable energy systems and green hydrogen production [1,2]. However, there are still some challenges to operate these cells during long-term operation as the cells work above 800 °C and face degradation problems [3,4]. During operation, these cells inside the stacks go through high thermo-mechanical loading scenarios such as thermal gradients due to difference in thermal cycles as well as mismatch of thermal expansion coefficients of different components. Several studies were performed to simulate these types of thermo-mechanical loading scenarios by testing at both cell and stack level [5–9].

Apart from thermo-mechanical testing, most of the studies were focused on the strength of both electrolyte and the cells for fuel electrode supported and electrolyte supported cells. The strength of the electrolyte was mostly determined by ring-on-ring tests (RoR) and ball-on-three-balls (B3B) tests [10–12]. The strength of both types of solid oxide cells was investigated by RoR tests [13], tensile tests [14,15], B3B tests [16,17] and four-point bending (4-PB) tests [18]. Recently, a tensile test with a novel gripping system for ultra-thin 3YSZ electrolytes (≤90 μm thick) was presented to test more volume of the specimen [19]. Moreover, studies such as tensile and shear joint strength tests [20–23] and 4-PB tests [24] were performed to determine the adhesion between metallic interconnectors and glass ceramic sealants. Furthermore, the interfacial fracture energy between the glass-ceramic sealant (V11) and Crofer 22 APU interconnects was evaluated by means of four-point bending tests [25] to measure the interfacial adherence at sealings in solid oxide cells. Later, a modified 4-PB test was developed to determine the adherence of the contact layer with the interconnector for better

---

[*] Corresponding author.
E-mail address: borhan.manam@uni-bayreuth.de (B.U. Manam).

https://doi.org/10.1016/j.ceramint.2025.10.069
Received 22 July 2025; Received in revised form 18 September 2025; Accepted 5 October 2025

electrical contact in solid oxide cells [26]. In another study, a three-point bending test was carried out based on the Schwickerath-crack-initiation-test as per ISO 9693 to determine the bonding strength and to understand the bonding mechanism (cohesion/adhesion) at the interface of electrode and interconnectors in solid oxide fuel cells [27]. The above-mentioned tests were applied to the interconnectors, where the thickness of specimens were more than 1 mm, which is not suitable for the interfacial adhesion testing of the ultrathin SOCs.

A key factor to extend the lifetime of the SOCs at the cell level is to improve the mechanical properties of the electrodes and the electrolytes. Thus, methodologies such as cross-sectional nano-indentation tests were introduced to calculate the elastic modulus and the hardness of NiO/YSZ based fuel electrodes, yttria stabilized zirconia (YSZ) and gadolinium doped ceria oxide (GDC) electrolytes and lanthanum strontium manganite (LSM) based air electrodes [28–31]. Surface micro-indentation and surface nano-indentation tests were intensively performed on the lanthanum strontium cobalt ferrite (LSCF) and LSCF/GDC based air electrodes to determine their elastic modulus and hardness [32–35].

Another key factor for the robustness of the cells is the interfacial adhesion between the electrode and the electrolyte for the robustness of the cells. The interfacial adhesion within the cell assembly needs to be sufficient to provide not only better electro-chemical performance but also improved mechanical strength during operation [36–38]. Hence, several studies were also carried out to evaluate the interfacial adhesion properties between electrodes and electrolytes. For that purpose, the interfacial fracture toughness between the air electrode and the electrolyte was determined by the four-point bending tests [39,40]. In another study, the Rockwell indentation tests were performed in the fuel electrode supported cells to calculate the interface adhesion between the fuel electrode and substrate as well as the interface toughness between the fuel electrode and electrolyte [41]. Furthermore, micro-scratch tests were performed to evaluate the interfacial adhesion of LSCF/GDC based air electrodes to YSZ electrolytes in an electrolyte supported cell where the electrolyte was 1 mm thick [35]. In that study, a progressive load up to 40 N was applied to detach the electrode coating from the electrolyte. Since the air electrode was sintered at 900 °C, which was lower than the typical sintering temperature of 1000–1300 °C, it did not demonstrate any detachment from the electrolyte, unlike typical brittle coatings.

Until so far, no work was reported to evaluate the interfacial adhesion within the membrane electrode assembly (MEA) of ultrathin electrolyte supported SOCs (140–150 μm). Thus, the aim of this study was to evaluate the hardness and elastic modulus of the porous electrode materials in as-sintered conditions by performing micro-indentation tests at different loads to get reliable values. Since it is difficult to extrapolate mechanical properties based on the dense materials for the porous electrodes where the porosity is more than 30 %, the instrumented micro-indentation technique was used to determine the elastic modulus and hardness of the electrode materials at micro-scale level. This represented the mechanical behavior of the electrodes. The as-sintered cells (pre-reduced) were investigated in this study as their mechanical properties are necessary for the further optimization of the manufacturing process and adhesion within the MEA of the cells for long-term operation. Further objectives were to evaluate the interfacial adhesion strength of the gadolinium doped ceria oxide (GDC) barrier layer with the 3 mol % yttria stabilized zirconia (3YSZ) electrolyte as well as the interfacial adhesion strength between the electrodes and 3YSZ electrolyte in the new ultrathin SOCs (140–150 μm) by scratch tests. The scratch tests were chosen because of their earlier application in multilayered ceramic coatings to determine the interfacial adhesion strength [42–44], whereas other test methods such as four-point bending test and Rockwell indentation test are not suitable for this type of ultrathin specimens as thicker specimens greater than 200 μm are needed for the implementation of valid tests. A relation between the interfacial adhesion strength and the hardness of the electrode materials was expected. Furthermore, scanning electron microscopy (SEM) analysis was performed to observe the adhesion failure morphology on the scratch surface at critical forces and energy dispersive spectroscopy (EDS) analysis was implemented to detect the Zr element distribution on the scratch track at the critical load. The obtained novel results in this work are a significant step forward to characterize the interfacial adhesion of ultrathin electrolyte supported SOCs (140–150 μm), where the mechanical properties and the interfacial adhesion properties of the fuel electrode and the air electrode were not investigated before, which will impact the further development of the electrode materials for long-term operation (>10,000 h).

2. Experimental

In this section the experimental details are discussed, which includes the tested materials, microstructure characterization, mechanical properties and interfacial adhesion testing.

2.1. Materials

Commercial solid oxide cells (SOCs) in as-sintered (pre-reduced) conditions (see Fig. 1) with a thickness of 140–150 μm were investigated in this study. The cells comprised of a gadolinium doped ceria oxide (GDC) barrier layer screen-printed on both sides of the 3 mol% yttria stabilized zirconia (3YSZ) electrolyte. The fuel electrode consisted of nickel oxide (NiO) and GDC. On the other hand, the air electrode was made of lanthanum strontium cobalt ferrite (LSCF) and GDC. The screen-printed electrodes were sintered at a minimum temperature of 1000 °C. The following as-sintered specimens were tested in this study.

a. GDC barrier layer screen printed on the 3YSZ electrolyte on the H_2 electrode side
b. GDC barrier layer screen printed on the 3YSZ electrolyte on the O_2 electrode side
c. Composite-H_2 consisted of fuel (H_2) electrode (NiO/GDC) + GDC barrier layer screen printed on the 3YSZ electrolyte on the H_2 electrode side
d. Composite-O_2 made of air (O_2) electrode (LSCF/GDC) + GDC barrier layer screen printed on the 3YSZ electrolyte on the O_2 electrode side

Fig. 1 (c) was the full cell, where one time it was used for scratching the fuel electrode composite and another time for scratching the air electrode composite. The tests of the fuel electrode composite and the air electrode composite were not conducted in the same specimen. Individual specimens were employed to perform the tests at fuel electrode composite and air electrode composite.

2.2. Microstructure characterization

Small fragments of the specimens were embedded with a resin (DuroCit-3, Struers, Denmark). After that, samples were ground and polished with a grinding machine (Tegramin 23, Struers machine, Struers, Denmark) with the final step with 0.05 μm colloidal silica. A scanning electron microscope (Zeiss Sigma 300 VP, Zeiss, Germany) was utilized for microstructural analysis, where the back-scattered electron (BSE) detector with an accelerating voltage of 15 keV was implemented to capture the different composition of each layer and to investigate the porosity inside the layers. An accelerating voltage of 20 keV was chosen for energy dispersive spectroscopy (EDS) elemental mapping on the scratched surface from the scratch test to verify the electrolyte exposure. Due to the roughness of the layers, the thickness of the total electrode was measured at five different points by analyzing the SEM images having a resolution of 18.1 pixels per μm for all the specimens with the Image-J software (National Institutes of Health, USA). The total porosity and the pore size of each layer was calculated with a machine learning algorithm (Trainable weka segmentation) with the Image-J software.

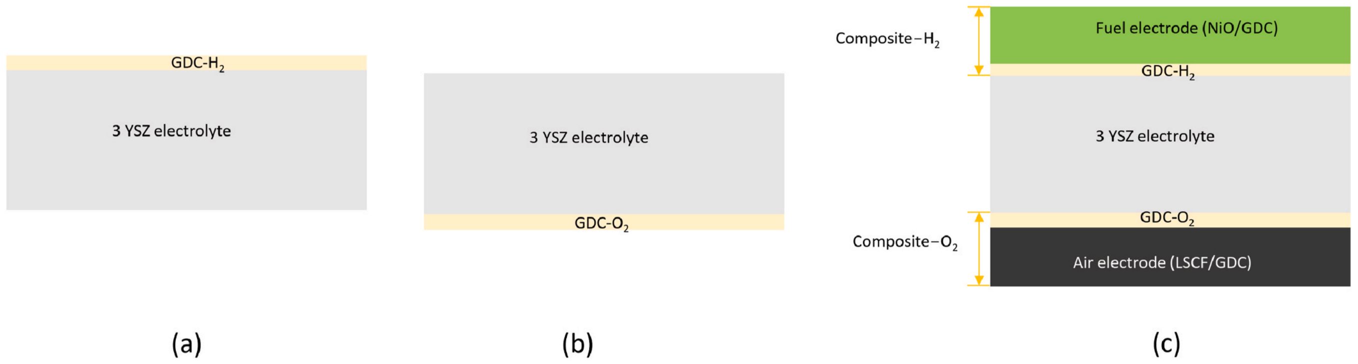

Fig. 1. Schematic of the tested layers in the solid oxide cell (SOC).

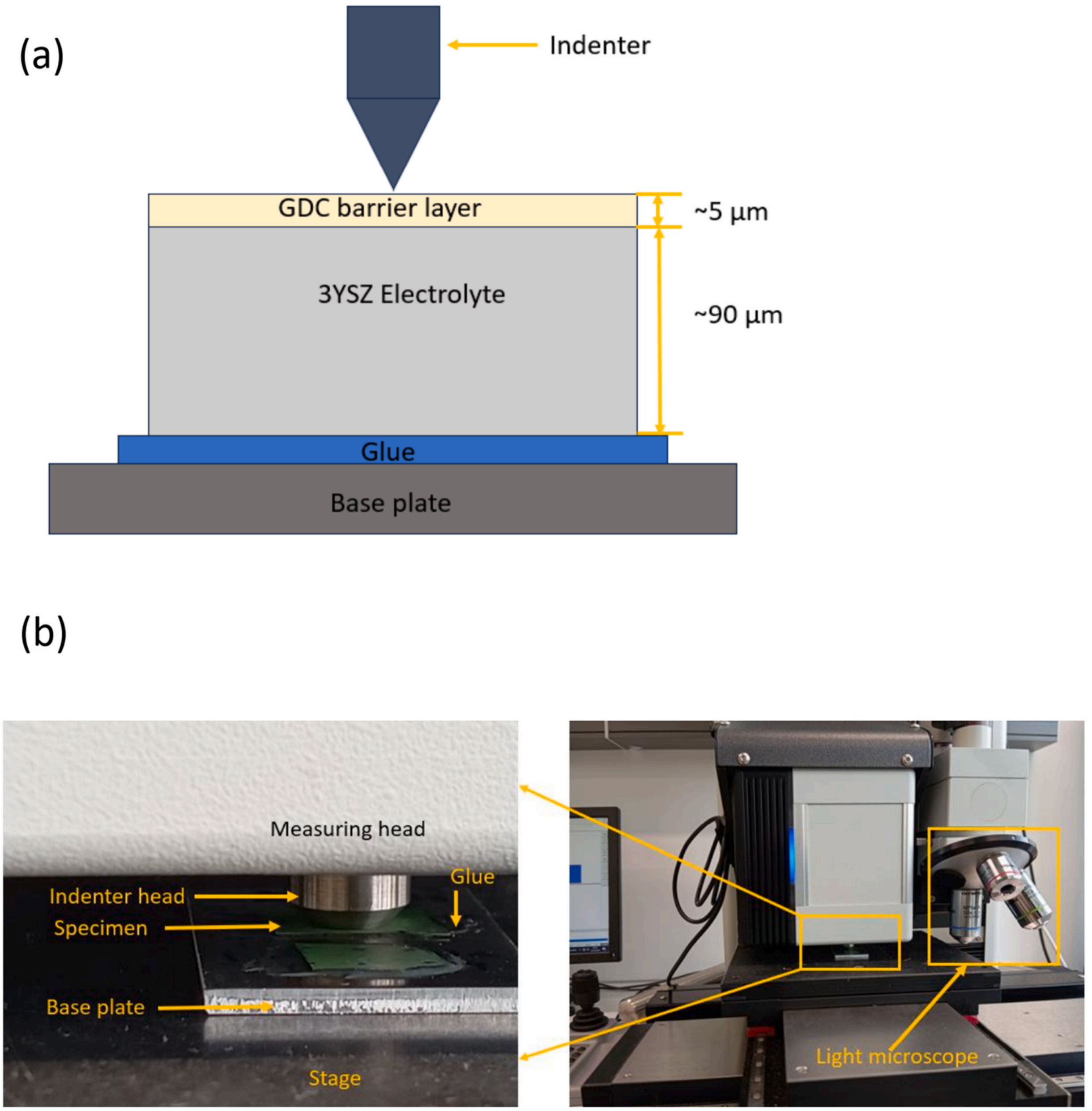

Fig. 2. (a) Schematic of the surface micro-indentation test; (b) experimental setup of the surface micro-indentation test.

For each of the layers, five images were analyzed. Beforehand, one image from each layer was trained with the algorithm to get the desired output.

2.3. *Mechanical properties with micro-indentation tests*

The mechanical properties elastic modulus E and hardness H were determined by a hardness testing machine (Fischerscope HM 2000, Helmut Fischer GmbH, Germany). The equipped probe was a four-sided Vickers pyramid indenter, which had a nominal tip radius of 500 nm and an angle of 136°. The Vickers indenter was selected as it was suitable for thick coatings (>1 μm), applicable for micro-scales and had a sharp tip similar to Berkovich indenter. However, Berkovich indenter was not used due to having a tip radius of 100 nm, applicable mostly in thin coatings less than 1 μm [45]. Furthermore, Knoop indenter was not applied due to having asymmetric indentation imprint [46].

The schematic and the experimental setup of the surface micro-indentation is illustrated in Fig. 2. The GDC barrier layers were thinner (3–5 μm) than the other layers. For this reason, indentation loads of 10 mN, 20 mN, 30 mN and 50 mN were chosen for these layers. Two small fragments of the GDC barrier layer bonded to the 3YSZ electrolyte from the fuel electrode composite and the air electrode composite were glued with a steel reinforced epoxy resin glue (JB Weld, USA) on the base plate. Ten valid indentations were considered for both specimens for the evaluation. Furthermore, two small fragments from the fuel electrode composite (composite-H_2) and the air electrode composite (composite-O_2) were tested with 100 mN, 200 mN, 300 mN and 500 mN, respectively. For each of the indentation loads, ten valid indentations were considered for the calculation of the elastic modulus and the hardness of the individual layers. To perform the valid indentation tests on the porous electrode material, the maximum indent depth h_{max} was kept within 30 % of the total thickness of the electrode to avoid the influence of the electrolyte [47,48]. The next two subsections describe the analytical formulation to calculate the elastic modulus and the hardness of the electrode materials.

2.3.1. *Elastic modulus E*

The elastic modulus of the specimens was calculated from the indentation load and indentation depth curve using the Oliver-Pharr method providing the material elastic and plastic properties [49]. The reduced elastic modulus E_r was determined from the unloading part of the curve by the following equation,

$$E_r = \frac{\sqrt{\pi}\cdot S}{2\cdot\sqrt{A_c}} \tag{1}$$

where S is the contact stiffness of the unloading part, which was determined from the slope of the unloading part of the curve $S = \left(\frac{\mathrm{d}P}{\mathrm{d}h}\right)_{h=h_{max}}$.

A_c is the projected contact area $= k\cdot h_c^2$; k is 24.5 for the Vickers indenter [31,46].

This reduced elastic modulus is defined as the combination of the elastic modulus of the indented material and the elastic modulus of the indenter.

$$\frac{1}{E_r} = \frac{(1-\nu_s^2)}{E_s} + \frac{(1-\nu_i^2)}{E_i} \tag{2}$$

where E_s is the elastic modulus of the indented material and $E_i = 1170$ GPa is the elastic modulus of the diamond indenter [50], respectively. $\nu_s = 0.3$ (assumed) and $\nu_i = 0.07$ [50] are the Poisson's ratio of the indented material and indenter, respectively.

The contact depth h_c was determined from the methodology proposed by Oliver and Pharr [49].

$$h_c = h_m - \varepsilon\cdot\frac{P_{max}}{S} \tag{3}$$

where h_m is the maximum indentation depth, P_{max} is the maximum indentation load and ε is the strain parameter, which is equal to 0.75.

2.3.2. *Hardness H*

The instrumented hardness H_{IT} considers the contact depth between the indenter and the indented material and the projected contact area. The H_{IT} was calculated from the methodology proposed by Oliver and Pharr [49],

$$H_{IT} = \frac{P_{max}}{A_c} \tag{4}$$

The elastic modulus and hardness were determined from the top 10 % of the unloading curve for the elastic regime from the indent load and depth curve to provide reliable results. The top 10 % of the unloading curve showed linear behavior and provided the best fitting for the slope of the unloading curve.

2.3.3. *Composite elastic modulus $E_{composite}$ and hardness $H_{composite}$*

This subsection describes the formulation to determine the elastic modulus and hardness of each composite.

By performing the micro-indentation tests, the elastic modulus and hardness of each individual layer of the electrode was determined considering the porosity. As the electrodes were multilayered coating systems like composites, the laminate theory or the rule of mixture (ROM) in the direction of layer thickness was applied. Thus, for the electrode composites, the elastic modulus $E_{composite}$ and hardness $H_{composite}$ were calculated using the ROM in the direction of the thickness [51].

$$E_{composite} = \frac{\sum_{i=1}^{n} E_i\cdot t_i}{\sum_{i=1}^{n} t_i} \tag{5}$$

$$H_{composite} = \frac{\sum_{i=1}^{n} H_i\cdot t_i}{\sum_{i=1}^{n} t_i} \tag{6}$$

where n is the number of layers added and t_i is the thickness of individual layer, E_i is the elastic modulus of the individual layer and H_i is the hardness of the individual layer, with $i = 1,2 \ldots, n$. The elastic modulus and hardness of the individual electrode layer depended on the porosity. The porosity dependent models according to Ref. [52,53], are as follows,

$$\text{Linear model}, E_i = E_0\cdot(1-bp) \tag{7}$$

$$\text{Nonlinear model}, E_i = E_0\cdot\left(1-\frac{bp}{1+(b-1)p}\right) \tag{8}$$

$$\text{Exponential model}, E_i = E_0\cdot exp(-bp) \tag{9}$$

$$\text{Exponential model}, H_i = H_0\cdot exp(-bp) \tag{10}$$

where E_0 is the elastic modulus of dense electrode material, H_0 is the hardness of the dense electrode material, p is the percentage of porosity and b is corresponding fitting parameter.

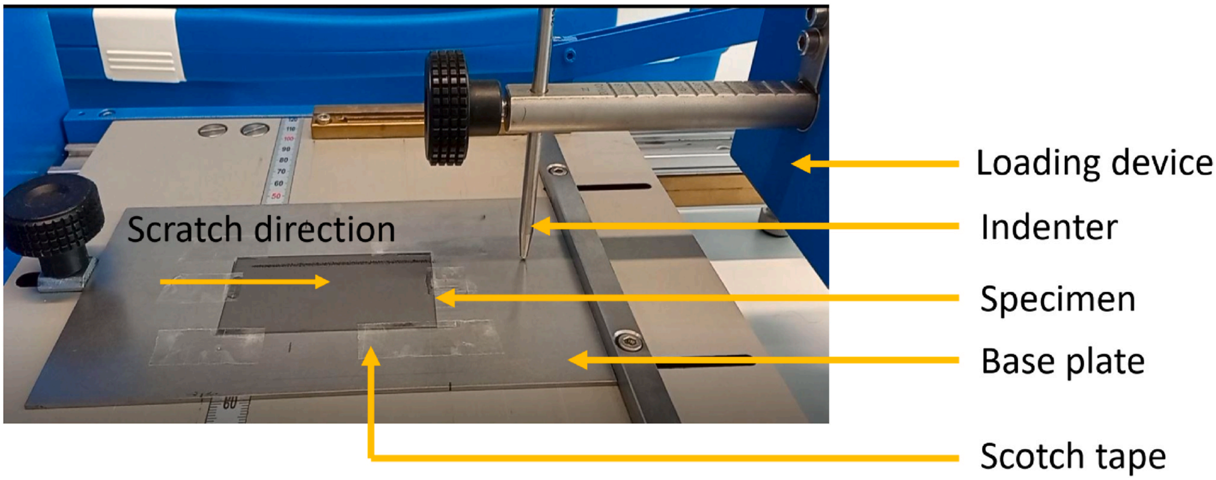

Fig. 3. Scratch test experimental setup.

2.4. *Interfacial adhesion testing with scratch tests*

The interfacial adhesion testing was carried out with a scratch testing machine (Erichsen Lineartester 249, ERICHSEN GmbH & Co. KG, Germany), as presented in Fig. 3. The scratching speed was 35 mm/s during the experiment. The employed indenter tip was made of a hard metal as per ISO 1518-1, where the scratch stylus “B” had a nominal diameter of 1 mm. This stylus was selected for representative scratches. The specimens had dimension of 40 × 70 mm^2. The specimens were attached with a scotch tape (Tesa SA, Switzerland) to glue with the base plate to avoid the movement of the specimens during scratch test. A minimum of nine specimens were tested with the scratch tests for reliable results and scratched at least three times with the same critical force for reproducibility, where the critical force was introduced with a normal dead load having a 0.5 N step-size. The critical force was defined as the force at which the electrode materials were detached from the 3YSZ electrolyte and the 3YSZ electrolyte was visible on the scratch track.

The shear stress model of Ollivier and Matthews [54] depending on the normal force was applied for the determination of the interfacial shear strength.

$$\tau = \frac{F_n}{\pi \cdot a \cdot \sqrt{R^2 - a^2}} \tag{11}$$

where τ is the shear strength (MPa), F_n is the normal force (N), R is the indenter tip radius (mm), a is the contact radius between the indenter tip radius and the coating (mm). For an approximate value $a \approx d/2$, d is the scratch width (mm).

The scratch width was measured perpendicular to the direction of the scratch track with a roughness device (MarSurf PS 10, Mahr, Germany). The scratch width was calculated from the raw data by utilizing the software Origin. A minimum of three measuring points on the scratch length was considered to measure the scratch width d and the corresponding contact radius a. A minimum of total eighty measuring points was considered to determine the interfacial shear strength of the specimens.

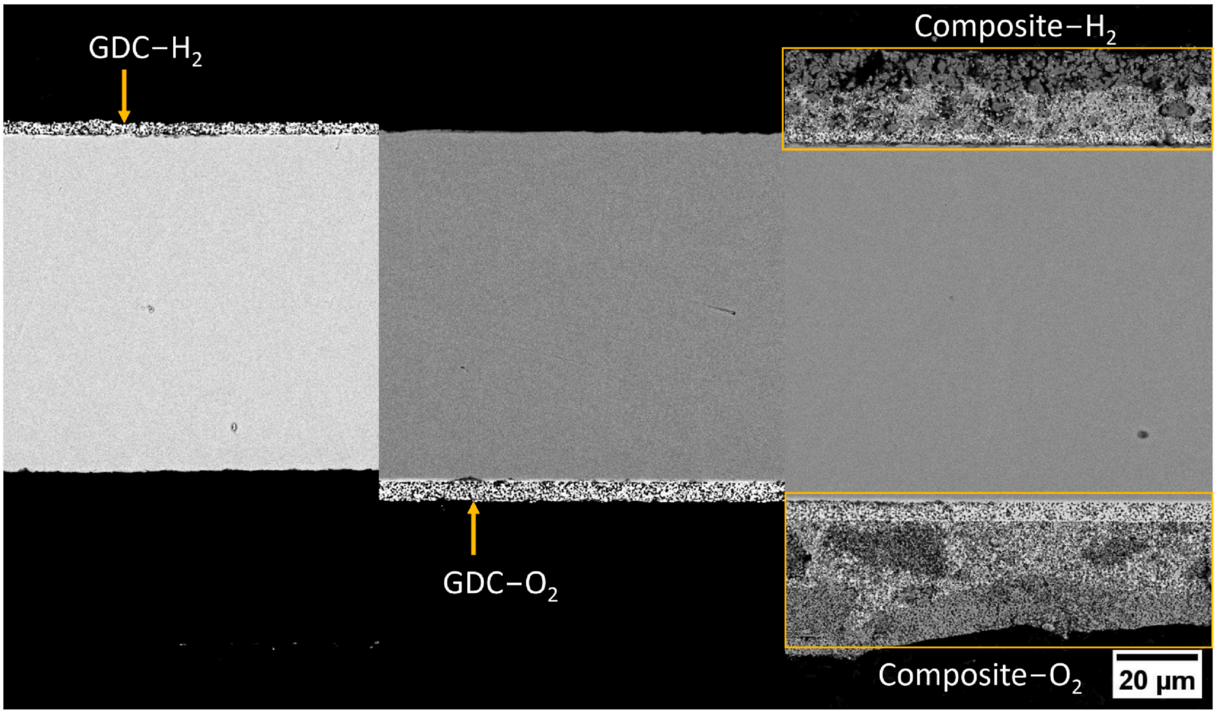

Fig. 4. Back scattered (BSE) micrograph of cross-section of the different layers of the electrodes.

3. Results and discussion

In this section the results obtained for the microstructure, mechanical properties and interfacial adhesion tests are discussed.

3.1. Microstructure characterization

The microstructure of the composites is displayed in Fig. 4. The measured thickness of the gadolinium doped ceria oxide (GDC) barrier layer, the fuel electrode and the air electrode were 3–5 μm, ~25 μm and ~30 μm, respectively. The calculated total porosity level of the GDC barrier layer and the electrodes was between 25 and 35 %.

The measured thickness of the GDC barrier layer was in good agreement with the thickness of the GDC barrier layer mentioned in Ref. [51]. Besides, the measured thickness of the GDC barrier layer in this study indicated that it was suitable enough to prevent undesired secondary phases such as $SrZrO_3$ [55]. Moreover, the measured thickness of the fuel electrode made of nickel oxide (NiO) and GDC (NiO/GDC) of approximately ~25 μm was comparable to the reported thickness of 25 μm for fuel electrode (Ni/GDC) in electrolyte supported cell, where the electrolyte consisted of yttria stabilized zirconia (YSZ) was 100 μm thick [56]. On the other hand, the measured thickness of the air electrode composed of lanthanum strontium cobalt ferrite (LSCF) and GDC (LSCF/GDC) of about ~30 μm was consistent with ref. [57]. For less ohmic and polarization losses of the cells, this thickness of 25–30 μm of the fuel electrode and the air electrode was required [55,58,59].

The segmentation process of the pores from the Image J software by using Trainable Weka Segmentation (TWS) is shown in Fig. 5. The calculated total porosity level of 25–35 % for both fuel and air electrodes were in good agreement with literature values where the reported total porosity of the fuel electrode (NiO/GDC) was 33.4 % according to Ref. [60] and the total porosity of the air electrode (LSCF/GDC) was 38 % according to Ref. [55]. As the cells were too thin, it was not possible to determine the total porosity of the individual layers by the Archimedes method or helium pycnometer. Hence, the total porosity was calculated by analyzing the SEM micrographs for the electrode composites. The determined total porosity level of the electrode materials using the Image-J software provided reliable results. The results were comparable to literature values. Furthermore, this level of total porosity of 25–35 % in electrode materials was necessary for electro-chemical activity i.e. sufficient gas diffusion and triple phase boundary to provide sufficient electro-chemical performance [59,61].

The pore size distribution of all layers is shown in Fig. 6 as boxplots. The average pore size was the mean value of pore diameter defined by Feret diameter, which was obtained from the analyzed images. The determined average pore size of the GDC barrier layer at the fuel electrode and the air electrode side was 0.68 μm and 0.80 μm, respectively. The measured average pore size of the NiO layer and the diffusion layer at the fuel electrode was 1.10 μm and 0.67 μm, respectively, whereas the average pore size of the LSCF layer and the diffusion layer at the air electrode side was 0.79 μm and 0.81 μm, respectively. The determined pore size of the GDC barrier layer at the fuel electrode size was less than the GDC barrier layer at the air electrode side, which provided better interfacial adhesion with the fuel electrode side mentioned in section 3.3. The pore size near the electrolyte should be smaller (less than 1 μm), which was observed at the GDC barrier layer near the electrolyte. The bigger pores were observed at the layer near the gas feed or the current collector layer. Pores larger than 1 μm are better for gas transport than the small pores, whereas small pores contribute to the triple phase boundaries. Thus, graded pore sizes were employed in the current solid oxide cells for better triple phase boundary and gas transport.

3.2. Mechanical properties

The indent load and indent depth curves obtained from the micro-indentation tests for the GDC barrier layer and the electrodes are depicted in Fig. 7(a)–(d). Although the curves differed from one another, such variations were expected for porous layers. The indent depth to electrode thickness ratio is presented in Fig. 8, whereas the indentation imprints after micro-indentation are displayed in Figs. 9 and 10. It is difficult to assume “ideal” impressions, but that this was not to be expected with porous materials. It can be seen from Fig. 7 (a) and (b) that the GDC barrier layers showed more elastic behavior than the other layers in the electrodes, as the dense GDC had a high elastic modulus of 214–223 GPa [30].

The calculated contact depth of the NiO layer as per equation (3) inside the fuel electrode for different indent loads was $h_c^{NiO} = 2.6 \pm 0.8$ μm whereas the determined contact depth of the LSCF layer inside the air electrode was $h_c^{LSCF} = 3.9 \pm 1.4$ μm. The contact depth was determined to measure the contact area as well as to present the elastic

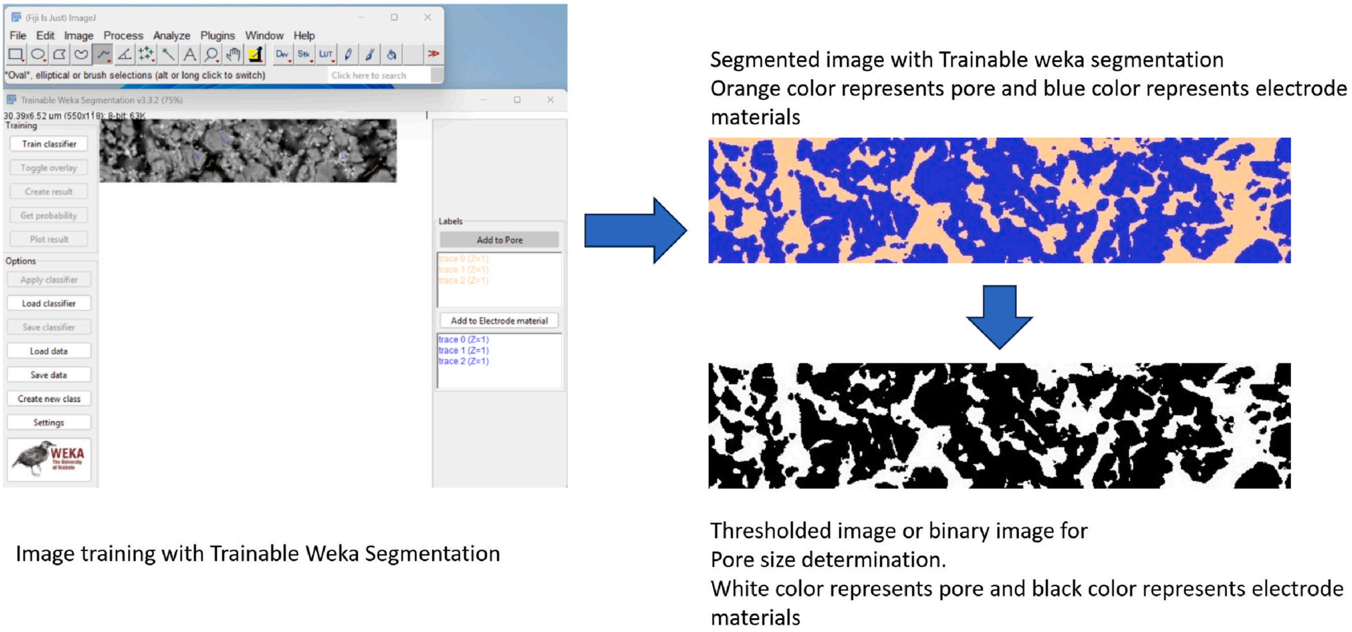

"Oval", elliptical or brush selections (alt or long click to switch)

Segmented image with Trainable weka segmentation
Orange color represents pore and blue color represents electrode materials

Image training with Trainable Weka Segmentation

Thresholded image or binary image for
Pore size determination.
White color represents pore and black color represents electrode materials

Fig. 5. Pore segmentation process from the SEM micrographs using Trainable Weka Segmentation (TWS).

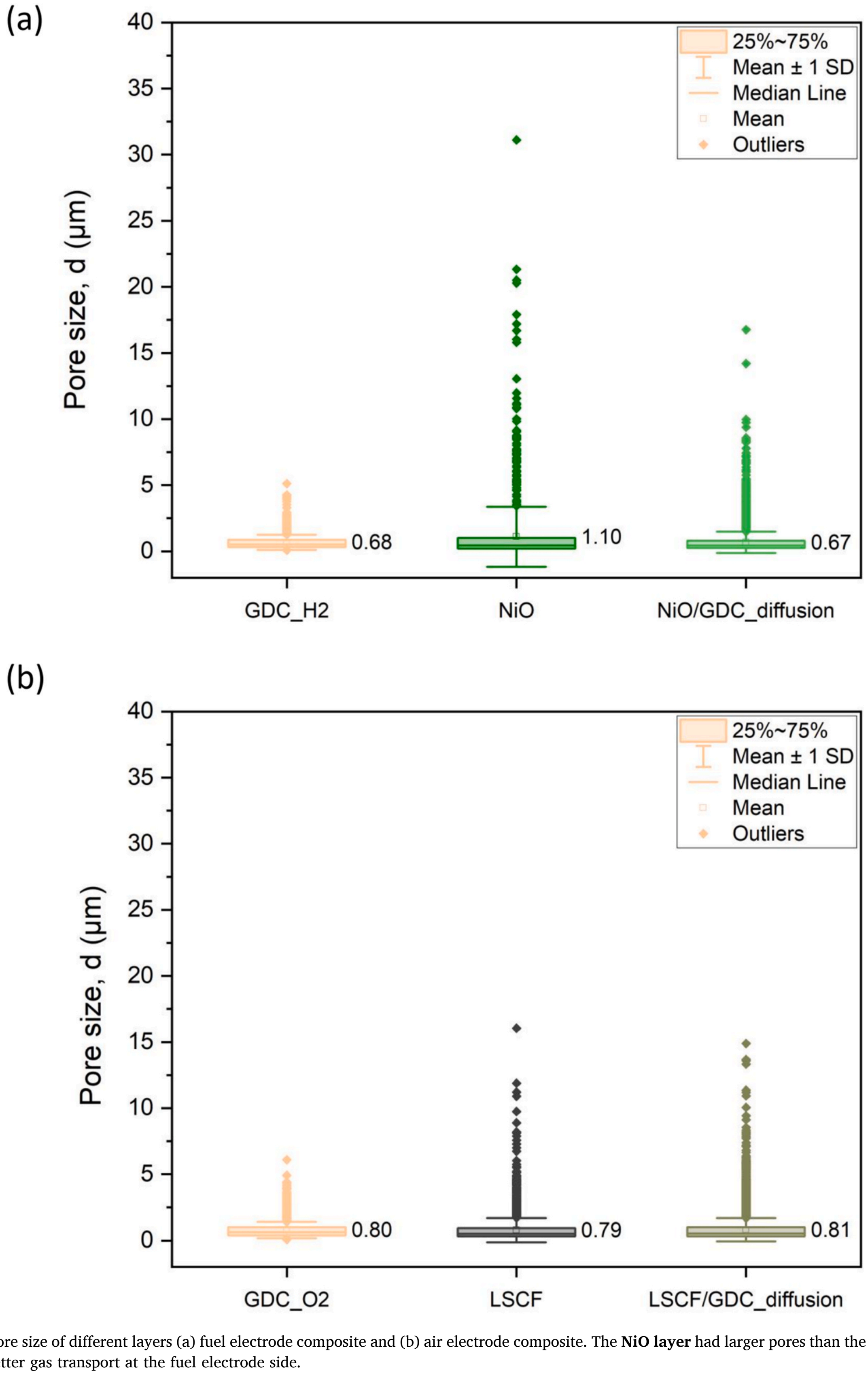

Fig. 6. Average pore size of different layers (a) fuel electrode composite and (b) air electrode composite. The **NiO layer** had larger pores than the **LSCF layer**, which was needed for better gas transport at the fuel electrode side.

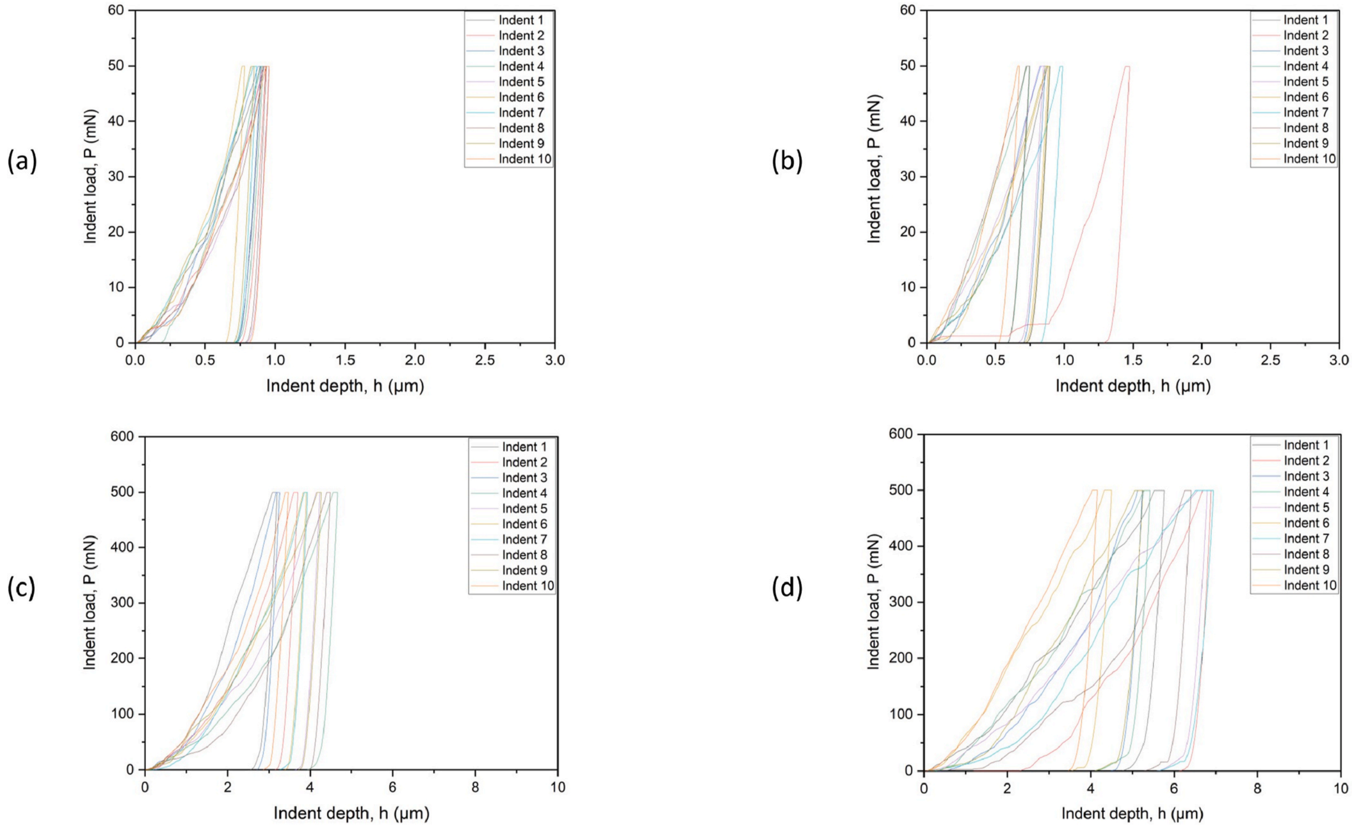

Fig. 7. Indent load vs. indent depth curves at 50 mN for (a) **GDC layer** of fuel electrode side, (b) **GDC layer** of air electrode side, at 500 mN for (c) **NiO** layer and (d) **LSCF layer** which illustrates the elastic responses of the electrode materials.

response of the electrode materials. The determined indent depth indicated that the NiO layer was 50 % more elastic than the LSCF layer inside the air electrode. The 50 % value was calculated from

$$\left(\frac{h_c^{NiO} - h_c^{LSCF}}{h_c^{NiO}}\right)\cdot 100\%$$

Moreover, the NiO layer was harder than the LSCF layer, which can be observed from the SEM micrographs of Fig. 10. The indentation imprint at the LSCF layer was ~3 times larger than the NiO layer. Magnified view of the indentation imprints is shown in Fig. 10.

The reason behind that the NiO layer was stiffer and harder than the LSCF layer is because NiO has a face cubic crystal structure, which influences its stiffness and resistance to deformation and cracking [62]. On the other hand, LSCF is a perovskite-structured oxide with oxygen vacancies and has mixed ionic-electronic conductive behavior, which makes it prone damage such as deformation, cracking [32,34]. An average of the elastic modulus and hardness values of the different layers is summarized in Table 1.

The determined values of the elastic modulus for the electrode materials are summarized using an exponential model of porosity depended elastic modulus and hardness as this model represented the real value of the porous electrode materials and showed good agreement with literature [52,53]. The calculated hardness of the GDC barrier layer was 4–4.6 GPa with a porosity level of ~35 % for the indentation load of 10–50 mN. The indentation loads of 10–50 mN were chosen as the GDC barrier layer was 10 times thinner than the other layers of the electrode. The earlier reported hardness value of the dense GDC electrolyte was 12.6–14.3 GPa with the indentation load of 10 mN [30].

The determined hardness of the NiO layer at the fuel electrode in this study was about 1.5 GPa for a total porosity level of about 35 % whereas, the reported hardness value for the dense NiO film was 4.1–9.7 GPa [62]. On the other hand, the calculated hardness of the LSCF contact layer at the air electrode was about 0.9 GPa for the total porosity level ~35 %. The hardness value was in good agreement with the earlier determined hardness of the LSCF contact layer about 0.6–1.3 GPa, where the porosity level was 24–40 % [32,33]. In that study, the hardness was measured by surface nano-indentation tests with a spherical and Berkovich indenter. Furthermore, the indent depth was 20 % of the electrode thickness [32]. The obtained hardness of the LSCF layer in this study with the Vickers indenter with the indent depth of 30 % of the electrode thickness was comparable to those values. The surface micro-indentation tests were selected instead of the cross-sectional indentation tests. In the cross-sectional indentation tests, the specimens were embedded in resin which penetrated the pores. This penetration of the resin reinforced the pores leading to inappropriate values of hardness and elastic modulus of the electrode materials.

The (NiO/GDC) fuel electrode consisted of a NiO current collector layer along with a functional layer of NiO and GDC mixture, which was the diffusion layer. This diffusion layer changes with time and temperature. The diffusion layer beneath the NiO layer was segmented using the Image-J software to determine the phase fraction of NiO, GDC and porosity. The determined phase fraction of NiO, GDC and porosity was ~53 %, ~27 % and ~20 %, respectively. By applying the exponential model of the elastic modulus and hardness depending on the porosity, the value of the elastic modulus and hardness of the diffusion layer was 102 ± 28 GPa and 2.9 ± 0.5 GPa, respectively. A reported Vickers hardness of NiO/GDC composite was 4.7–5.3 GPa for the load of 5–20 N, however the level of porosity was not mentioned [63]. The determined value of 2.9 GPa in the present study was indeed comparable to the fuel electrode supported cell, where the functional layer was made of NiO-8YSZ and had a hardness value of 4.12 GPa [29]. In that study, a cross-sectional nano-indentation test was performed [29].

In a similar manner, the diffusion layer of the air electrode,

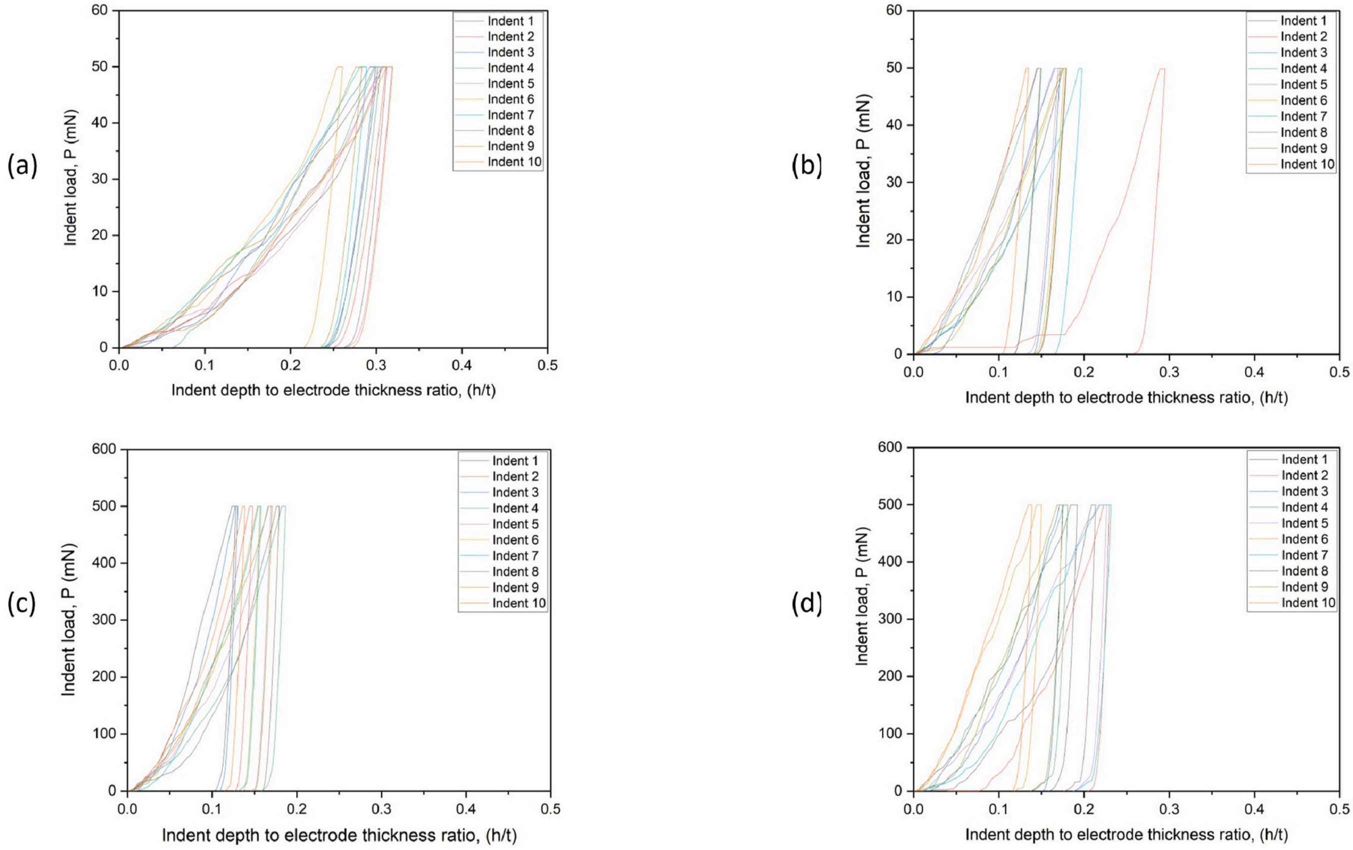

Fig. 8. Indent depth within 30 % of the total electrode thickness for (a) **GDC barrier layer** for fuel electrode side and (b) **GDC barrier layer** for air electrode side at indent load of 50 mN; (c) **NiO layer** and (d) **LSCF layer** at indent load of 500 mN.

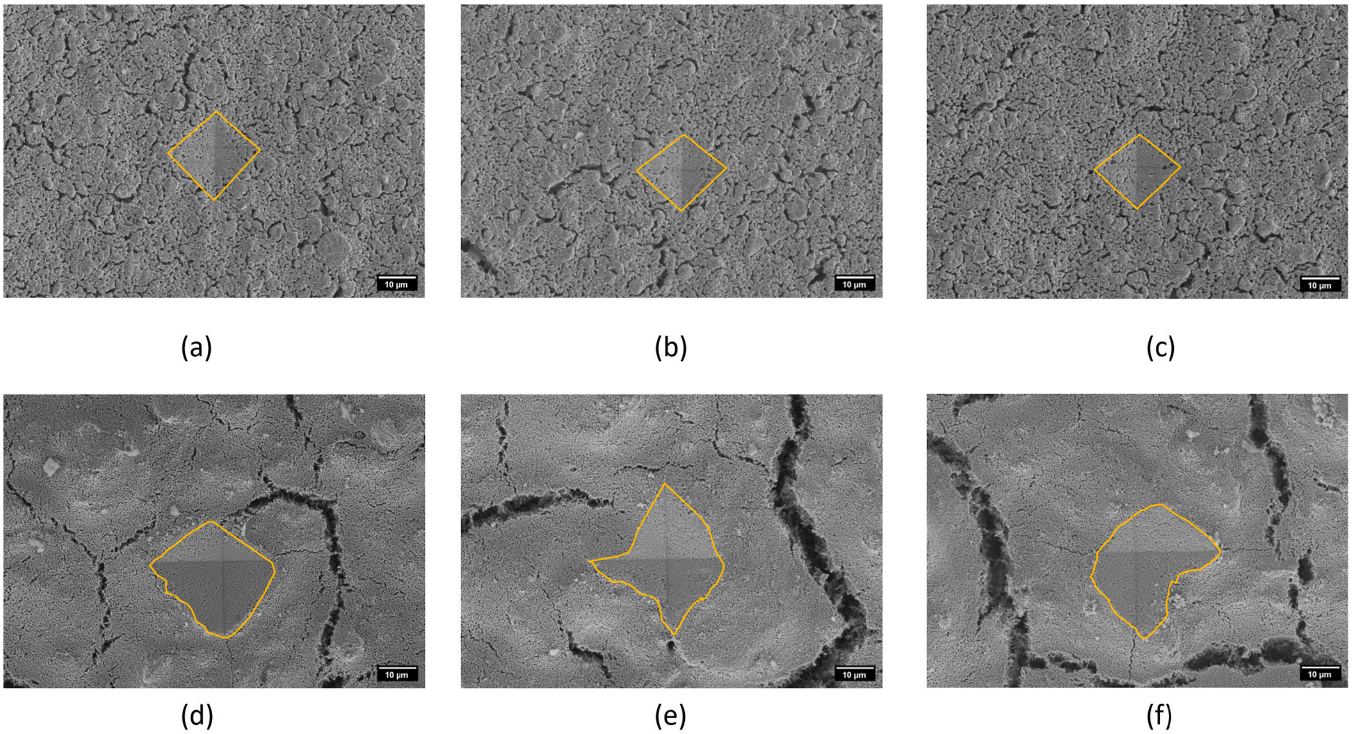

Fig. 9. Multiple indents at various locations (a) to (c) on the **NiO layer** and (d) to (f) on the **LSCF layer**. It can be seen that the indents on the **LSCF layer** were larger than the **NiO layer**.

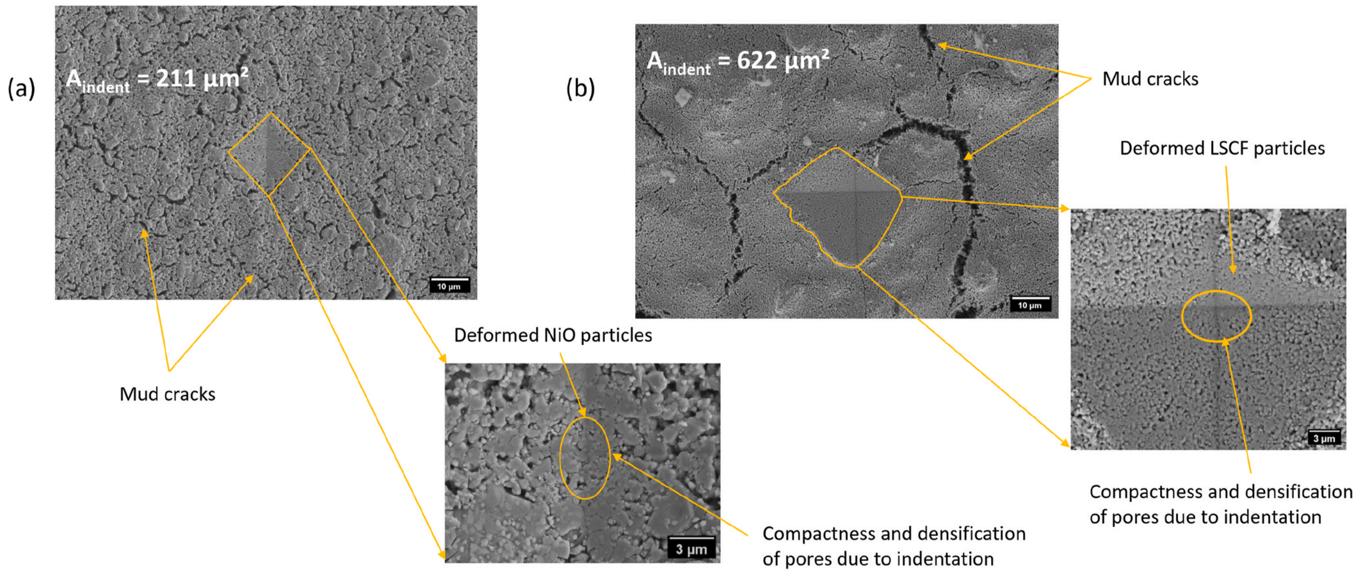

Fig. 10. Magnified view of indentation imprint of (a) **NiO layer** and (b) **LSCF layer** for the indentation load of 500 mN. The LSCF layer had a larger imprint area than the NiO layer, which indicated that the LSCF layer was softer than the NiO layer.

Table 1
Elastic modulus and hardness of the individual layer of the electrodes. The presented values are mean values with standard deviation.

Layer	No. of indents per indent load	Indent load P_{max} (mN)	Elastic modulus E (GPa)	Hardness H (GPa)
GDC-H_2	10	10, 20, 30, 50	107 ± 20	4.0 ± 2.2
GDC-O_2	10	10, 20, 30, 50	115 ± 22	4.6 ± 2.0
NiO	10	100, 200, 300, 500	79 ± 12	1.6 ± 0.4
LSCF	10	100, 200, 300, 500	46 ± 11	0.8 ± 0.4

composed of a mixture of GDC and LSCF and situated under the LSCF layer as the (LSCF/GDC) air electrode consisted of the LSCF contact layer and the diffusion layer. The phase fractions of LSCF, GDC and porosity were determined through image segmentation using ImageJ software, yielding values of ~51 %, ~13 % and ~36 %, respectively. Applying the exponential model of porosity dependent elastic and hardness, the elastic modulus and hardness of the diffusion layer were calculated to be 63 ± 3 GPa and 1.4 ± 0.1 GPa, respectively. The hardness value of the LSCF/GDC composite from the previous studies was about 8.1–9.8 GPa, which had a relative density of 94–98 % [64]. In another study, the hardness of the LSCF/GDC composite was 8.05–9.34 GPa for the total porosity level of 1.5–8.3 % [65]. The determined elastic modulus and hardness of the fuel electrode (NiO/GDC) applying the rule of mixture was 93 ± 17 GPa and 2.4 ± 0.4 GPa, respectively, whereas the calculated elastic modulus and hardness of the air electrode (LSCF/GDC) implementing the rule of mixture was 54 ± 2 GPa and 1.0 ± 0.1 GPa, respectively.

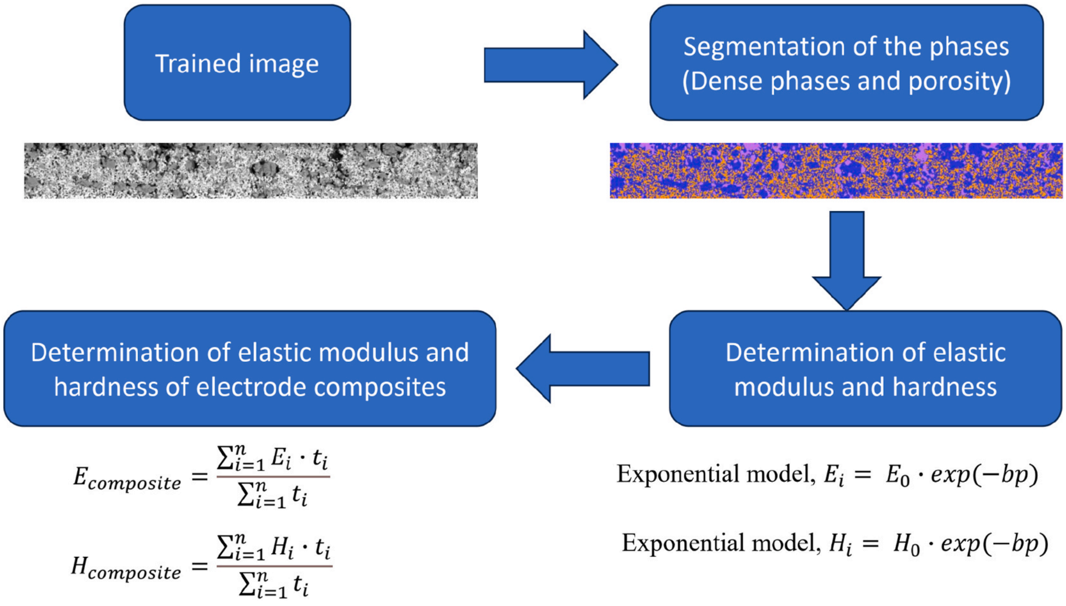

$$E_{composite} = \frac{\sum_{i=1}^{n} E_i \cdot t_i}{\sum_{i=1}^{n} t_i}$$

$$H_{composite} = \frac{\sum_{i=1}^{n} H_i \cdot t_i}{\sum_{i=1}^{n} t_i}$$

$$\text{Exponential model, } E_i = E_0 \cdot exp(-bp)$$

$$\text{Exponential model, } H_i = H_0 \cdot exp(-bp)$$

Fig. 11. Workflow of determination of elastic modulus and hardness of the diffusion layer and electrode composites.

Table 2
Elastic modulus and hardness of the composites as per rule of mixture.

Composite	Layers	Elastic modulus *E* (GPa)	Hardness *H* (GPa)
Composite-H$_2$	Fuel electrode (NiO/GDC) + GDC-H$_2$	96 ± 15	2.7 ± 0.6
Composite-O$_2$	Air electrode (LSCF/GDC) + GDC-O$_2$	64 ± 2	1.6 ± 0.3

The segmentation technique was implemented to calculate the elastic modulus and the hardness of the diffusion layer of the fuel electrode and the air electrode depending on the porosity as it was not possible to directly perform the surface indentation method on the diffusion layers, see Fig. 11. By applying equations (5) and (6), the elastic modulus and hardness of the composites are presented in Table 2.

It can be noticed from Table 2 that the composites of the electrode material were softer than the GDC layer itself. The contribution of the GDC barrier layer inside both electrodes in terms of hardness was ~28 % and ~50 % for the composite-H$_2$ and composite-O$_2$, respectively. The rule of mixture (ROM) was applied as the electrodes were multilayered coating systems equivalent to composite materials. Besides, a model to evaluate the hardness of the multilayered coatings was proposed by performing the nano-indentation method [66]. In that study, the ROM was implemented. Thus, in the present study, a simplified version of that model was adopted to calculate the hardness of the electrode composites.

The achieved results of the elastic modulus and the hardness of the fuel electrode composite (composite-H$_2$) and the air electrode composite (composite-O$_2$) would not only contribute to the further optimization of the manufacturing of cells but also to determine the stress conditions at the individual layers using simulations. Besides that, the obtained values of the elastic modulus and hardness of the electrodes are important to determine the fracture toughness of the cell and the strength of the cells depending on the test methods. Furthermore, the sintering conditions of each individual layer could be optimized for better mechanical properties and robustness of the cells. Table 3 shows the comparison of the mechanical properties of the electrode materials with the current electrode materials.

3.3. Scratch test results

The interfacial adhesion of electrode materials with the electrolyte is crucial for the mechanical stability and electro-chemical performance of the cells. For the durability of the cells, it is necessary that the cells do not go through delamination, wear or spallation. Thus, scratch tests were performed to determine the interfacial adhesion properties between the GDC barrier layer and the 3YSZ electrolyte as well as the interfacial adhesion between the fuel electrode composite/3YSZ and air electrode composite/3YSZ.

Table 3
Comparison of electrode materials with previous studies.

Electrode	*Porosity (%)*	*E* (GPa)	*H* (GPa)	P_{max} (mN)
NiO-SDC [41]	N/A	168[b]	4.1[c]	100[b], 2940[c]
NiO-YSZ/YSZ [28]	N/A	182–204	6.82–7.29	20.1
NiO-YSZ [29]	27	107	4.12	10
NiO-GDC [63]	N/A	N/A	4.7–5.3	5–20 N
LSCF-GDC [64]	2–6	119–153	8.9–10.8	30–490
LSCF-GDC [65]	1.5–8.3	N/A	8.05–9.34	1 kg
LSCF [32]	15.2–46.9	32.4–121.5	0.37–1.97	50–500
LSM [29]	N/A	21.12	0.71	10
GDC [30]	dense	186–239	10.5–16.9	5–500
GDC[a]	25–35	107–115	4.0–4.6	10–50
NiO[a]	25–35	79 ± 12	1.6 ± 0.4	100–500
(NiO/GDC)/GDC[a]	25–35	96 ± 15	2.7 ± 0.6	100–500
LSCF[a]	25–35	46 ± 11	0.8 ± 0.4	100–500
(LSCF/GDC)/GDC[a]	25–35	64 ± 2	1.6 ± 0.3	100–500

[a] This work, b is the indent load for elastic modulus and c is the indent load for hardness.

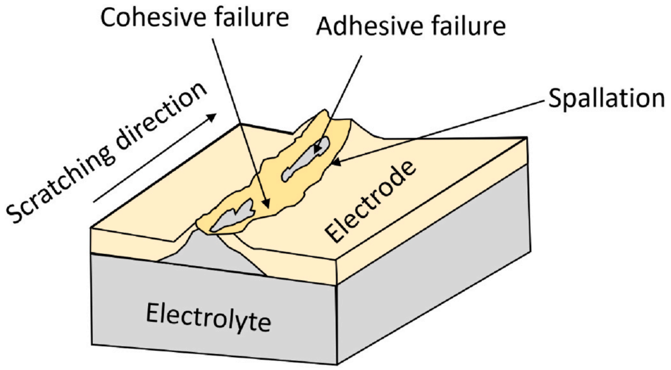

Fig. 12. Schematic of the failure modes in electrode and electrolyte after scratch test.

The observed failure modes after the scratch testing are illustrated in Fig. 12 and the specimen after scratch testing at different normal forces and the scratch width for the critical force are displayed in Fig. 14(a) and (b). The scratches before the critical normal force is shown in Fig. 13. The BSE micrographs of different electrode materials at critical forces, where the electrode materials were detached from the 3YSZ electrolyte to expose the electrolyte at the scratch track after scratch testing are presented in Fig. 14(c)–(f). It can be seen from the SEM micrographs Fig. 14(c)–(f) that the GDC barrier layers had the strongest adhesion to the electrolyte compared to the other electrode materials.

From Fig. 14(c)–(f) it can be noticed that the dominant failure mode was spallation which is associated with the detachment of the electrode materials from the electrolyte. The electrode materials exhibited both adhesive and cohesive failure. The cohesive failure occurred within the electrode materials and the adhesive failure was the separation of the electrode materials from the electrolyte.

In general, the spallation failure is specified as the detachment of the coating from the substrate. But the electrode composites were a multilayered coatings system, thus the spallation failure in this study was attributed not only to the detachment of the electrode materials from the electrolyte but also to the separation of the electrode materials from the underlaying electrode layer. Hence, the spallation failure behavior within the electrode materials was known as cohesive spallation failure and the adhesive spallation failure was defined as the failure when the electrolyte was visible on the scratch track.

For the verification of the 3YSZ electrolyte exposure, the EDS mappings were performed on the scratch track, which are provided in Fig. 15. The GDC barrier layer on the fuel electrode side exhibited better interfacial adhesion than the air electrode side as the GDC barrier layer on the air electrode side. It can be assumed that the GDC barrier layer of the air electrode side was thicker than the fuel electrode side. The thicker GDC barrier layer on the air electrode side resulted in slightly less (~15 %) interfacial shear strength than the fuel electrode side as the critical force was less than the fuel electrode side. The better interfacial adhesion was also noticed at the fuel electrode composite (composite-H$_2$) than the air electrode composite (composite-O$_2$). The electrolyte at the fuel electrode composite (composite-H$_2$) was visible with the critical force of 13 N. On the other hand, for the air electrode composite (composite-O$_2$) the electrolyte was seen at 10 N, which was 23 % less than in comparison to the fuel electrode composite. This implies that the higher the critical force, the higher the interfacial shear strength between the GDC/3YSZ barrier. Moreover, depending on the critical force, the interfacial shear strength was determined by applying equation (11). The interfacial shear strength for the GDC barrier layer and the different composites are presented in Table 4.

It can be noticed from Table 4 that the GDC barrier layer had the

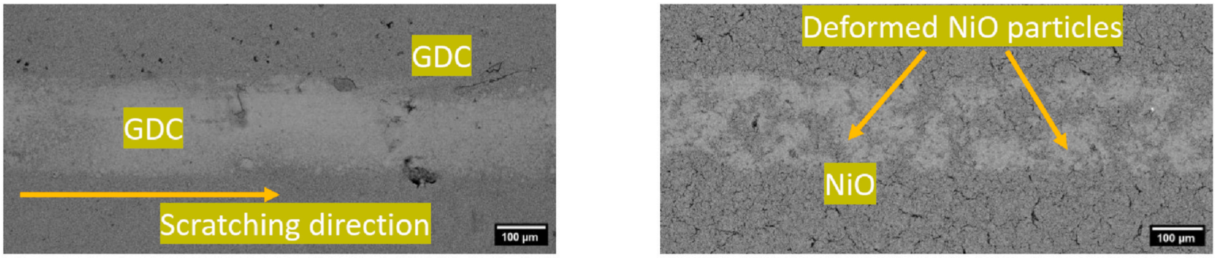

(a) GDC_H_2 at $F \leq 36$ N

(b) Composite–H_2 at $F \leq 12$ N

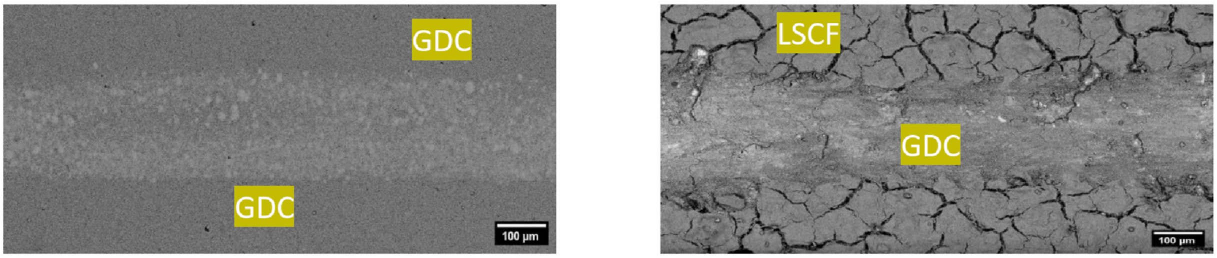

(c) GDC_O_2 at $F \leq 32$ N

(d) Composite–O_2 at $F \leq 7$ N

Fig. 13. Scratch morphology of the specimens lower than the critical force to expose the 3YSZ electrolyte. No 3YSZ electrolyte was visible before the critical force.

highest interfacial shear strength of $\tau = 243$–274 MPa as the critical force was highest. It can be further observed that the standard deviations at the GDC barrier layers were higher than the electrode composites due to the scattering of the scratch widths as the layers were porous. As the contact radius was dependent on the scratch width, the high deviation of the scratch width led to the high deviation of the interfacial shear strength. To minimize the deviation of the interfacial shear strength, one approach could be to measure more points (>6) on the single scratch track. Another reason was that the minimum scratch width was less than 100 µm, implying contact radius less than 50 µm and the maximum scratch width was greater than 500 µm indicating contact radius greater than 250 µm, which was also responsible for the greater deviation of the scratch width resulting in the deviations of the interfacial shear strength of the GDC barrier layer.

But with the addition of (NiO/GDC) fuel electrode layer on top of the GDC barrier layer, the interfacial shear strength with the electrolyte decreased to 52 MPa (− 81 %). One of the reasons behind the decrease in the interfacial shear strength was the increase of the tested area with the addition of the layers on top of the GDC barrier layer. Analogous to Griffith's theory, when the fiber is thinner, it had less defects and better mechanical properties. By contrast thick fibers have more defects, which results in decrease in mechanical properties [67]. Considering this theory, the GDC barrier layer alone had better interfacial shear strength than the electrode composites. It was due to the tested area being small, and the defects were less in contrast to the fuel electrode composite (composite-H_2) where the tested area was larger, indicating more defects. Moreover, the fuel electrode was also porous. The scratched area (product of scratched width and scratched depth) on the GDC barrier layer of the fuel electrode side was 575 ± 303 μm^2. On the other hand, the scratched area of the fuel electrode composite (composite-H_2) was 11,679 ± 4200 μm^2, which was more than 20 times than the scratched area of the GDC barrier layer. It indicated that the interfacial adhesion of fuel electrode composite/3YSZ significantly decreased with the deposition of the fuel electrode (NiO/GDC) on the GDC barrier layer. Thus, the GDC layers demonstrated the highest interfacial shear strength compared to the fuel electrode composites (composite-H_2). A similar phenomenon was found on the air electrode side. With the addition of the (LSCF/GDC) air electrode layer on top of GDC barrier layer, the interfacial shear strength of the air electrode composite/3YSZ was reduced to 47 MPa (− 80 %) due to the increase of the tested area with the addition of the air electrode. The scratched area of the GDC barrier layer on the air electrode side was 1099 ± 326 μm^2 compared to the scratched area of the air electrode composite, which was 10,507 ± 2105 μm^2. The scratched area increased tremendously by a factor of 10 with the addition of the air electrode layer on top of the GDC barrier layer leading to a significant decrease of interfacial adhesion.

Another reason for the reduction of the interfacial shear strength was the elastic mismatch ratio between the electrode materials and the 3YSZ electrolyte. The elastic mismatch ratio is defined by $\left(E_{electrode\ materials}/E_{3YSZ\ electrolyte}\right)$, where $E_{electrode\ materials}$ is the elastic modulus of the electrode materials and $E_{3YSZ\ electrolyte}$ is the elastic modulus of the 3YSZ electrolyte. The elastic mismatch ratio between the coating and substrate should be close to 1 to avoid delamination and for better interfacial fracture energy [68,69]. Thus, the elastic mismatch between the GDC barrier layer and the 3YSZ electrolyte was 0.51–0.55 taking the values from Table 1, whereas the elastic mismatch between the fuel electrode composite (composite-H_2) and the 3YSZ electrolyte was 0.46, applying the value from Table 2. The elastic mismatch of the air electrode composite (composite-O_2) and the 3YSZ electrolyte was 0.30 using the value from Table 2. The elastic mismatch of 0.55 indicated that the GDC barrier layer and the 3YSZ electrolyte had similar stiff behavior which indicated better interfacial adhesion. It was also found in the present study. On the other hand, the elastic mismatch of 0.46 suggested that the fuel electrode composite (composite-H_2) was less elastic than the 3YSZ electrolyte which implied moderate interfacial adhesion. Similarly, the elastic mismatch of 0.30 meant that the elastic modulus of the air electrode composite (composite-O_2) was significantly lower than the elastic modulus of the 3YSZ electrolyte ($E_{3YSZ} = 210$ GPa [70]). This suggested that the air electrode composite (composite-O_2) had less interfacial adhesion than the fuel electrode composite (composite-H_2) and the GDC barrier layer, which was observed in the present study.

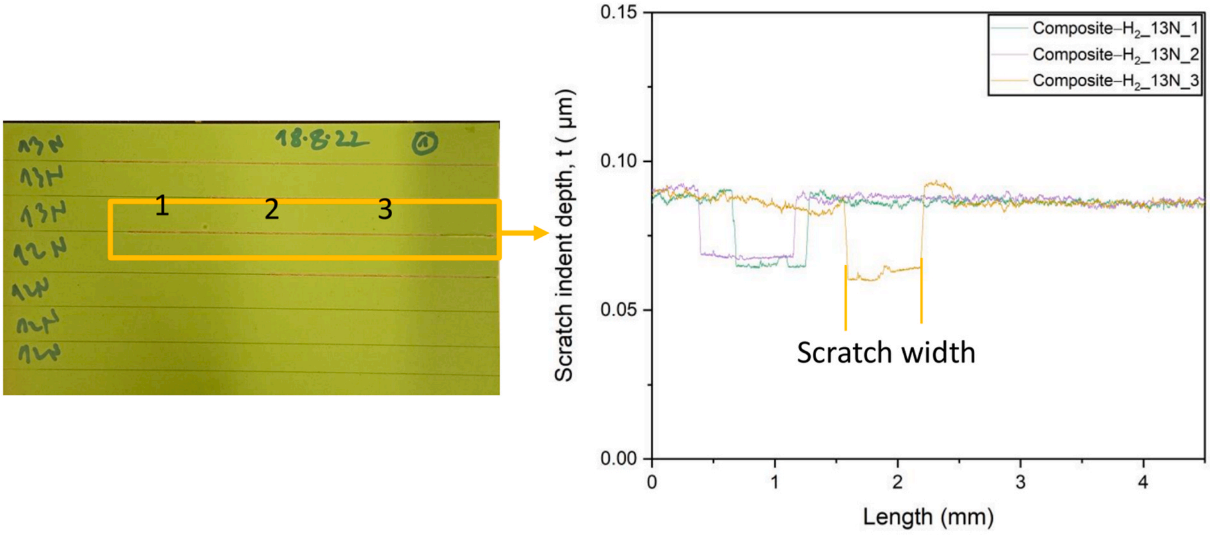

(a)

(b)

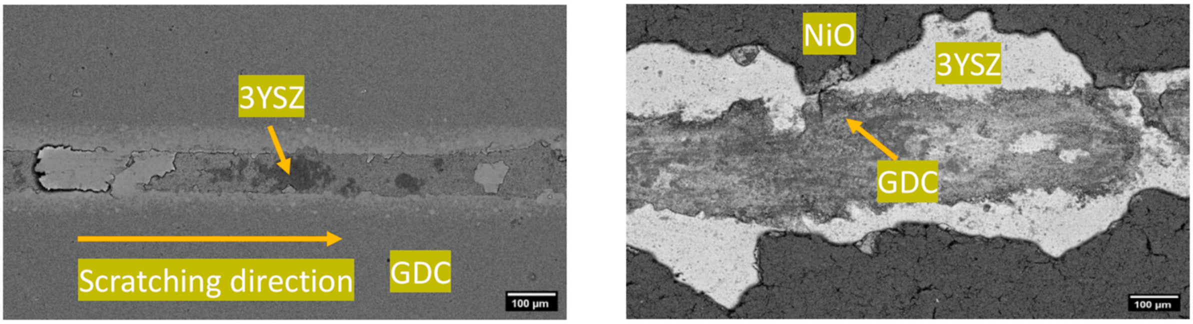

(c) GDC–H_2 at $F_{crit.}$ = 40 N

(d) Composite–H_2 at $F_{crit.}$ = 13 N

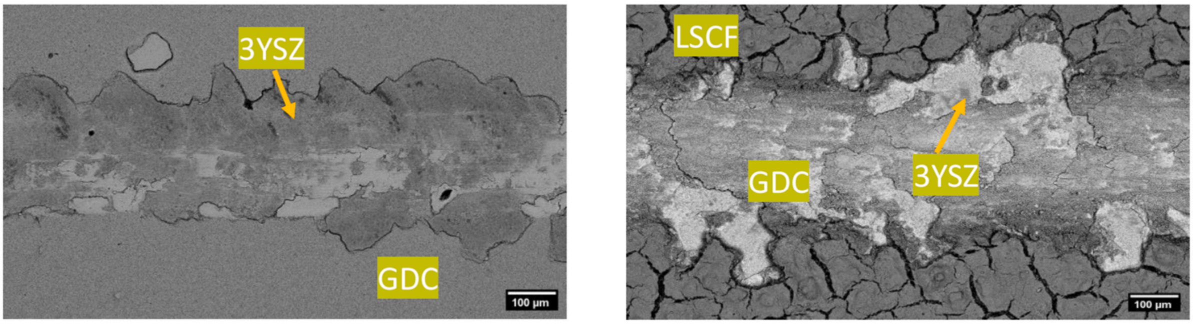

(e) GDC–O_2 at $F_{crit.}$ = 36 N

(f) Composite–O_2 at $F_{crit.}$ = 10 N

Fig. 14. (a) Specimen after scratch test at different normal forces (composite-H_2); (b) scratch width measuring process from profilometer data using the software Origin and (c) to (f) scratch surface morphology at critical normal force to expose the electrolyte (BSE micrograph). The SEM micrographs show the failure behavior (spallation) of the electrode materials.

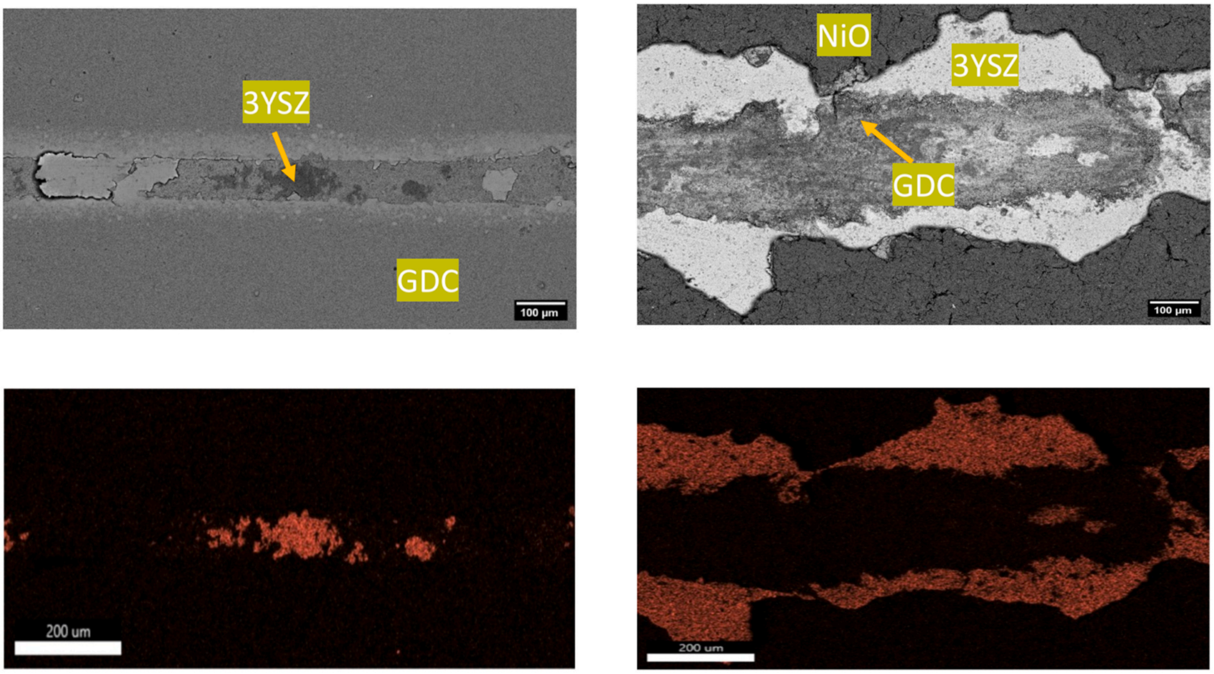

(a) GDC–H_2 at $F_{crit.}$= 40 N

(b) Composite–H_2 at $F_{crit.}$ = 13 N

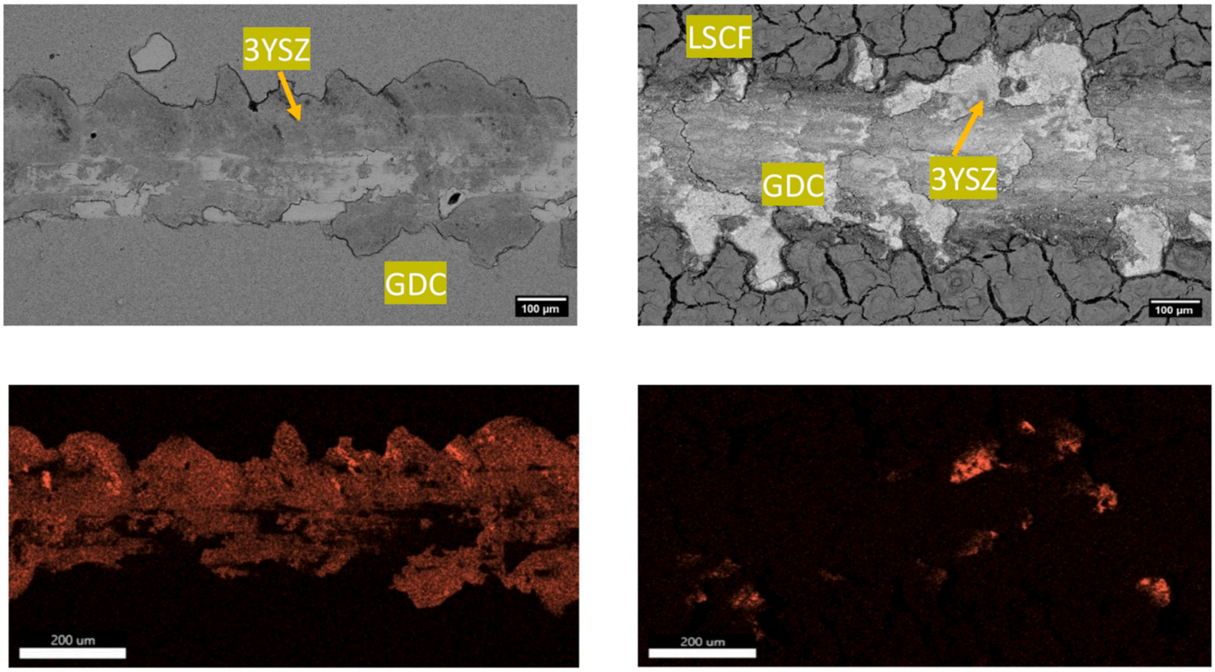

(c) GDC–O_2 at $F_{crit.}$= 36 N

(d) Composite–O_2 at $F_{crit.}$ = 10 N

Fig. 15. EDS mapping of detecting red = Zr element on the scratch track after scratch test at critical normal force, which verifies that at a certain critical force the electrolyte is exposed. (For interpretation of the references to colour in this figure legend, the reader is referred to the Web version of this article.)

Table 4
Critical force and interfacial shear strength of the GDC barrier layer and different composites. The presented values are mean values with standard deviation.

Layer / composite	No. of specimens	Critical force ***F*** (N)	Contact radius ***a*** (μm)	Shear strength ***τ*** (MPa)
GDC-H_2	10	40 ± 1	120 ± 40	274 ± 97
GDC-O_2	9	34 ± 2	105 ± 27	243 ± 75
Composite-H_2	9	13 ± 1	240 ± 85	52 ± 13
Composite-O_2	12	10 ± 1	161 ± 26	47 ± 7

Further reason for the reduction of the critical force and the interfacial shear strength was related to the hardness of the GDC barrier layer and other electrode materials. The GDC barrier layer had a higher hardness value of 4.6 GPa than the fuel electrode composite (2.7 GPa) and the air electrode composite (1.6 GPa). The higher hardness value indicated less plastic deformation of the electrode materials, which implied that high force was required for the fracture of the electrode materials. Thus, a higher load of 34–40 N was applied for the fracture of the GDC barrier layer. The fuel electrode composite went through more plastic deformation and showed spallation failure with the 3YSZ electrolyte for the critical force $F \geq 13$ N. Similar spallation failure of the air electrode with the electrolyte was noticed for the critical force $F \geq 10$ N. The air electrode composite started to fail with a less critical force due to the softness of the air electrode composite than the fuel electrode composite and the GDC barrier layer.

Moreover, a correlation between the hardness of the electrode materials and the interfacial shear strength was established, which is presented in Fig. 16. It was due to both testing methods involved normal forces. It can be noted from Fig. 16 that with the increase of the hardness, the interfacial shear strength increased as the interfacial shear strength was directly proportional to the critical force, presented in equation (11).

Furthermore, the elastic-plastic index, the H^3/E^2 ratio of the GDC barrier layer was 5.6–7.4 MPa and the fuel electrode composite and the air electrode composite were 2.1 MPa and 1.0 MPa, respectively. The elastic-plastic index indicates material's resistance to plastic deformation. Thus, the values suggested that the interfacial adhesion and the scratch resistance of the GDC barrier layer would be higher than the fuel electrode composite and the air electrode composite. Higher H^3/E^2 ratio led to less plastic deformation and better resistance to crack formation, which implied better adhesion of the coating with the substrate [71].

Further reason behind the reduction of the adhesion strength by adding the fuel electrode or the air electrode on the GDC barrier layer was because the layers were porous which created crack propagation easily inside the electrodes during scratching. Moreover, the interface between the electrodes and the GDC barrier layer was also porous. For which these crack propagations penetrated through the GDC layer, where the GDC barrier layer itself porous. Since the volume increased with the addition of the electrodes, the overall hardness of the composite decreased because of the addition of porous electrodes. Thus, the overall electrode composite showed less interfacial adhesion strength than the GDC barrier layer.

Additionally, the electrode materials behaved like laminated composites for which the deposited layers decreased the elastic modulus and hardness of the electrode composites. The contribution comes from different thicknesses of the electrode material. If the porous NiO or LSCF layer has less thickness than the GDC layer, the main contribution of the composite hardness will be carried by the GDC layer. If the thickness of the NiO or LSCF layer ≫ GDC layer, then the contribution of the composite hardness will be carried by the NiO or LSCF layer, which means, the composite hardness would be less than the GDC barrier layer. This was observed in the current study.

Besides, the added NiO and LSCF layers had "mud cracks". Those mud cracks might have initiated the cracks inside the electrodes and the GDC barrier layer during scratching, see Fig. 17. Thus, with less normal forces, the GDC barrier layer along with the electrodes detached from the 3YSZ electrolyte.

Finally, the residual stresses at the interface might influence the interfacial shear strength between the electrode composite and the

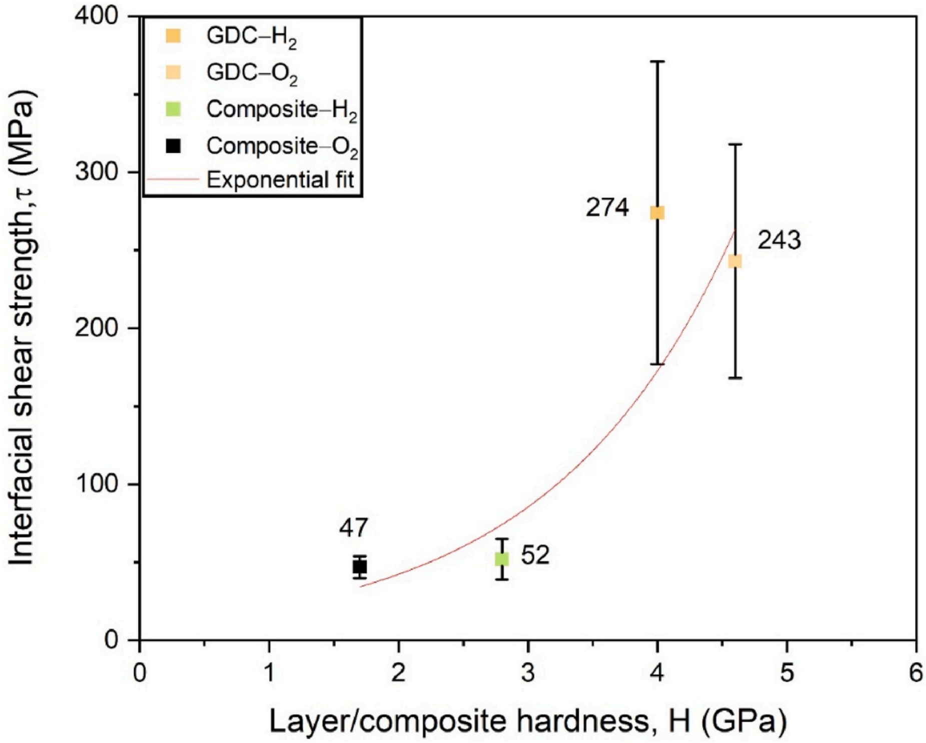

Fig. 16. Correlation between composite hardness and interfacial shear strength of GDC/3YSZ, fuel electrode composite/3YSZ and air electrode composite/3YSZ. The interfacial shear strength increases with the increase of hardness of electrode materials.

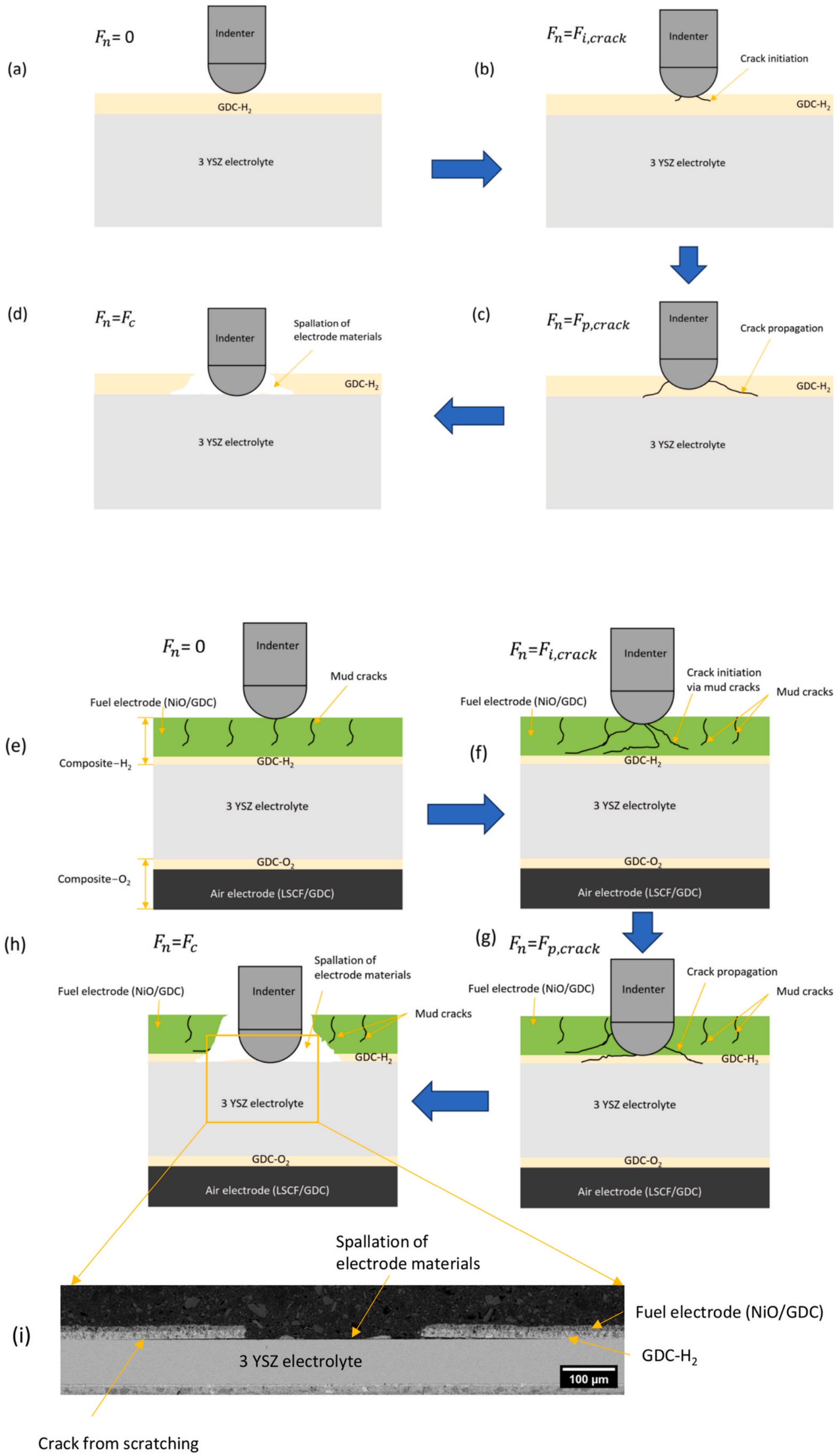

Fig. 17. Failure process of the GDC barrier layer (a) to (d) and fuel electrode composite with the addition of fuel electrode on the GDC barrier layer (e) to (h) during scratching, where F_n = normal force, $F_{i,crack}$ = normal force for crack initiation, $F_{p,crack}$ = normal force for crack propagation and F_c = critical normal force for spallation of GDC/electrode materials; (i) cross-section of fuel electrode composite after scratching (BSE image).

electrolyte. However, it was very difficult to determine the residual stresses induced during the sintering process. It was because the electrode materials and the interface were porous. For which accurate measurement of the residual stresses from X-Ray diffraction (XRD) was difficult due to the penetration of the signals through the porous electrodes. Furthermore, numerical simulation might be applicable but for that tangential force was needed, which was a limitation of the employed device in the present study. However, an approximation of the thermal residual stress during cooling down after sintering around 1000 °C was provided. The residual thermal stress was calculated according to Ref. [72] by the following equation,

$$\sigma_{TRS} = \left(\alpha_s - \alpha_f\right) \cdot \frac{E_f}{1 - \nu_f} \cdot (T_2 - T_1) \tag{12}$$

where σ_{TRS} is the residual thermal stress induced by the cooling of the electrode materials after sintering, α_s and α_f are the thermal expansion coefficients (CTE) of the electrolyte and electrode materials, respectively, E_f and ν_f is the elastic modulus and Poisson's ration of the electrode materials, $T_1 = 298$ K and $T_2 = 1273$ K are the room temperature and the sintering temperature of the electrode material, respectively. The applied respective CTE and sintering temperature are summarized in Table 5.

The CTE value of the fuel electrode (NiO/GDC) consisted of the CTE value of the NiO layer of 13.7×10^{-6} K^{-1} [74] and the diffusion layer (mixture of NiO and GDC) value of 13.59×10^{-6} K^{-1} [75], which were determined by the rule of mixture. In a similar manner the CTE of the air electrode (LSCF/GDC) was determined, where LSCF layer had CTE value of 16.9×10^{-6} K^{-1} [64] and the CTE value of the diffusion layer (mixture of LSCF and GDC) was 16.1×10^{-6} K^{-1} [64]. The residual thermal stress at the interface between the GDC barrier layer and the 3YSZ electrolyte yielded compressive stress of −304 MPa, which implied the GDC barrier layer had strong interfacial adhesion with the 3YSZ electrolyte. The estimated residual stress between the fuel electrode (NiO/GDC) and GDC barrier layer was +122 MPa and the residual stress between the (LSCF/GDC) and GDC barrier layer was about +290 MPa, which indicated the air electrode had larger residual tensile stress after deposition and prone to delamination and cracking than the fuel electrode. The wider mud cracks were observed in the air electrode than the fuel electrode.

A schematic along with the residual thermal stresses in the GDC barrier layers and the electrodes are shown in Fig. 18. Because of the residual tensile stress between the electrodes and the GDC barrier layer, less normal force was needed to spall the electrodes from the electrolyte. Although the GDC barrier layer had high compressive residual stress, the early delamination of the electrodes with less forces initiated early spallation of the GDC barrier layer at certain areas while scratching with less normal forces. It has to be mentioned that the curvature and the associated internal stress were not calculated due to lack of data from the cell manufacturer as the exact sintering parameter and conditions were not provided.

The obtained interfacial shear strength of the fuel electrode composite and the air electrode composite were calculated from the Ollivier and Matthews model, where only a single coating to a substrate system was assumed and only the critical normal force could be applied [54]. The model was implemented due to the absence of tangential force since the employed scratch test device was equipped only with a normal force sensor. As the tangential force was not considered, which might influence the results, by providing information of friction coefficient, which plays an important role in the scratching behavior of the material. However, the interfacial adhesion calculation in this study was based on the normal force only. Furthermore, the interfacial shear strength values of the individual measuring points were local values of the corresponding measuring points.

Table 5
Considered elastic modulus, Poisson's ratio and CTE for residual thermal stress calculation.

Layers	Elastic modulus E (GPa)	Poisson's ratio υ	CTE α ($\times 10^{-6}$ K^{-1})
GDC	115	0.3 (assumed)	12.7 [64]
3YSZ	210 [70]	0.27 [51]	10.8 [73]
NiO/GDC	93	0.3 (assumed)	13.6
LSCF/GDC	54	0.3 (assumed)	16.6

It also has to be mentioned that no literature values were available, where the interfacial adhesion properties were estimated within the membrane electrode assembly (MEA) in the electrolyte supported cells. In earlier studies, the interfacial fracture toughness was evaluated by four-point bending tests between the air electrode (LSM) and the electrolyte (YSZ) [39] and by Rockwell indentation tests between the anode (NiO/SDC) and electrolyte (SDC) [41].

In another study, the anode support exhibited better interfacial bonding with the interconnector than the air electrode [27]. Moreover, in a parametric study by implementing numerical investigation, the interfacial fracture energy between the electrolyte (YSZ) and the air electrode (LSM) was found to be slightly better than the interfacial fracture energy between the electrolyte (YSZ) and the fuel electrode (Ni/YSZ) [76]. In that study, the fuel electrode was in reduced conditions. The cells mentioned in the above studies were anode-supported solid oxide cells with different materials, but from a qualitative point of view based on the above-mentioned literature, the air electrode had less interfacial adhesion with the electrolyte than the fuel electrode in as-sintered condition. Thus, considering this perspective, the similar pattern was found in the present study, where the fuel electrode had better interfacial adhesion than the air electrode with the electrolyte.

The above-mentioned results in this work are a significant step forward to characterize the interfacial adhesion testing of the ultrathin SOCs (140–150 μm) because the values of the interfacial adhesion between the electrode composites and the electrolyte were not evaluated before. Compared with the state-of-the-art methods such as 4-PB tests and Rockwell indentation tests, the scratch testing performed in this work had a simple test setup, were easy to perform and suitable for the electrolyte supported solid oxide cells. While the 4-PB test required stiffeners which have to be glued to both sides of the electrodes leading to inappropriate results and suitable for fuel electrode supported SOCs thicker than 200 μm [39,40]. On the other hand, the Rockwell indentation tests required very high loads [41]. Those high loads led to Hertzian cone fracture of the dense electrolyte in electrolyte supported SOCs. Furthermore, it was suitable for the fuel electrode supported SOCs, where the thicker (0.8 mm) porous fuel electrode substrate was capable of withstanding high loads [41]. Moreover, the progressive load mode micro-scratch tests demonstrated the measurement of the adhesion between the air electrode and the electrolyte [35]. That study proved that scratch testing was suitable for the electrolyte supported SOCs. However, the air electrode (LSCF/GDC) did not show the typical brittle fracture as it was sintered at 900 °C. In that study [35], the sintering temperature was less than the sintering temperature of 1000–1300 °C in the current work. Additionally, no separation of the LSCF coating from the YSZ electrolyte was observed [35].

In the present study, the scratch tests showed successfully their suitability for ultrathin electrolyte supported SOCs (140–150 μm). The constant load mode scratch tests provided novel results with valuable insights such as the correlation between the interfacial adhesion and the hardness of the electrode materials. These results would contribute to the further improvement of the interfacial adhesion between the electrode materials and the electrolyte for better electro-chemical performance of the cell at the interface. Better interfacial adhesion would lead to better stack performance for the desired power output in fuel cell mode and the desired green hydrogen production in electrolysis mode.

For further studies, progressive load mode scratch tests could be carried out, which would provide information about the tangential force. In the present study, the equipped scratch test device was confined

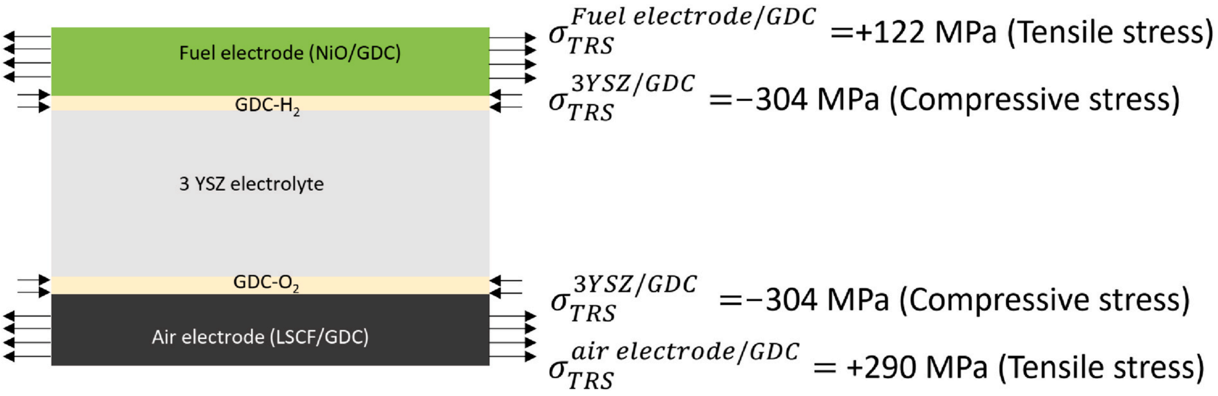

Fig. 18. Residual thermal stress on the fuel electrode, GDC barrier layers and the air electrode. Fuel electrode and air electrode were in tensile stress, whereas the GDC barrier layers were in compression.

to normal forces. Based on both tangential and normal force, it might be possible to evaluate the interfacial fracture toughness between the electrode materials and the electrolyte.

4. Conclusions

The present study dealt with the mechanical properties such as elastic modulus and hardness of electrode materials and the interfacial adhesion strength between the electrode materials and the electrolyte in the 3 mol% yttria stabilized zirconia (3YSZ) electrolyte supported solid oxide cells. The key conclusions of the current study are as follows:

- The mechanical properties of porous, thin gadolinium doped ceria oxide (GDC) barrier layer were determined for the first time. It had the highest elastic modulus of 107–115 GPa and hardness of 4.0–4.6 GPa than the fuel composite ($E = 96 \pm 15$ GPa and $H = 2.7 \pm 0.6$ GPa) and air electrode composite ($E = 64 \pm 2$ GPa and $H = 1.6 \pm 0.3$ GPa).
- The total porosity level of the fuel and air electrode composite were 25–35 %. The nickel oxide (NiO) layer at the fuel electrode composite had the largest average pore size of 1.10 μm, which was needed for better gas transport.
- Interfacial shear strength GDC/3YSZ, fuel electrode composite/3YSZ and air electrode composite/3YSZ were determined for the first time, yielding values of 243–274 MPa, 52 MPa and 47 MPa, respectively.
- A relation between hardness and interfacial adhesion was established, which indicated the higher the hardness of the electrode material is, the higher is the interfacial shear strength.
- A decrease in interfacial shear strength of 80 % between the electrode composites and the 3YSZ electrolyte was observed compared to the interfacial shear strength of GDC/3YSZ. It was because of the increased tested area, decrease in elastic mismatch as well as hardness of the electrode materials with the addition of porous electrode layers on the GDC barrier layer. Moreover, the decrease in the elastic-plastic index H^3/E^2 ratio of the electrode materials led to the reduced interfacial shear strength.

The results achieved in this study for the as-sintered cells were crucial for both the mechanical and electro-chemical prospects for long-term operation of the cells. The findings provided information on the mechanical and interfacial adhesion properties of the as-sintered cells before going through the reduction process. Furthermore, it would contribute to the optimization of the manufacturing process of the cells i.e. the sintering and joining process of the individual layers of electrode materials for long-term hours of operation.

CRediT authorship contribution statement

Borhan Uddin Manam: Writing – review & editing, Writing – original draft, Methodology, Investigation, Conceptualization. **Nico Langhof:** Writing – review & editing, Supervision, Resources, Methodology, Investigation, Funding acquisition, Conceptualization. **Carolin Sitzmann:** Writing – review & editing, Supervision, Resources, Methodology, Investigation, Funding acquisition. **Stefan Schafföner:** Writing – review & editing, Supervision, Resources, Funding acquisition.

Declaration of competing interest

The authors declare that they have no known competing financial interests or personal relationships that could have appeared to influence the work reported in this paper.

Acknowledgement

The authors greatly acknowledge the financial support from the German Federal Ministry of Research, Technology and Space (BMFTR) within the framework of the flagship project H$_2$Giga, project “HTEL-Stacks – ready for gigawatt”, via the grant number 03HY124D. The authors are grateful to Kerafol – Keramische Folien GmbH & Co. KG, Germany to laser cut the specimens. The authors also acknowledge the support from their colleague, Felix Wich for grinding and polishing of the specimens for microstructure inspection. The authors would also like to thank the Chair of Metals and Alloys, University of Bayreuth, for providing the facility to conduct the micro-indentation tests with their hardness testing device Fischerscope HM 2000, Helmut Fischer GmbH, Germany.

References

[1] R.M. Ormerod, Solid oxide fuel cells, Chem. Soc. Rev. 32 (2003) 17–28, https://doi.org/10.1039/B105764M.
[2] A. Hauch, R. Küngas, P. Blennow, A.B. Hansen, J.B. Hansen, B.V. Mathiesen, M. B. Mogensen, Recent advances in solid oxide cell technology for electrolysis, Science 370 (6513) (2020) eaba6118, https://doi.org/10.1126/science.aba6118.
[3] M.S. Khan, S.B. Lee, R.H. Song, J.W. Lee, T.H. Lim, S.J. Park, Fundamental mechanisms involved in the degradation of nickel–yttria stabilized zirconia (Ni–YSZ) anode during solid oxide fuel cells operation: a review, Ceram. Int. 42 (2016) 35–48, https://doi.org/10.1016/j.ceramint.2015.09.006.
[4] M.S. Khan, X. Xu, R. Knibbe, Z. Zhu, Air electrodes and related degradation mechanisms in solid oxide electrolysis and reversible solid oxide cells, Renew. Sustain. Energy Rev. 143 (2021) 110918, https://doi.org/10.1016/j.rser.2021.110918.
[5] J. Laurencin, B. Morel, Y. Bultel, F. Lefebvre-Joud, Thermo-mechanical model of solid oxide fuel cell fed with methane, Fuel Cells 6 (1) (2006) 64–70, https://doi.org/10.1002/fuce.200500096.
[6] J. Malzbender, R.W. Steinbrech, Advanced measurement techniques to characterize thermo-mechanical aspects of solid oxide fuel cells, J. Power Sources 173 (1) (2007) 60–67, https://doi.org/10.1016/j.jpowsour.2007.07.072.

[7] B.X. Huang, V. Vasechko, Q.L. Ma, J. Malzbender, Thermo-mechanical properties of (Sr,Y)TiO$_3$ as anode material for solid oxide fuel, J. Power Sources 206 (2012) 204–209, https://doi.org/10.1016/j.jpowsour.2012.01.137.

[8] H.S. Noh, K.J. Yoon, B.K. Kim, H.J. Je, H.W. Lee, J.H. Lee, J.W. Son, Thermo-mechanical stability of multi-scale-architectured thin-film-based solid oxide fuel cells assessed by thermal cycling tests, J. Power Sources 249 (2014) 125–130, https://doi.org/10.1016/j.jpowsour.2013.10.101.

[9] Y. Xiang, Y. Da, Z. Zhong, N. Shikazono, Z. Jiao, Thermo-mechanical stress analyses of solid oxide fuel cell anode based on three-dimensional microstructure reconstruction, Int. J. Hydrogen Energy 45 (38) (2020) 19791–19800, https://doi.org/10.1016/j.ijhydene.2020.05.121.

[10] F. Fleischhauer, R. Bermejo, R. Danzer, A. Mai, T. Graule, J. Kuebler, High temperature mechanical properties of zirconia tapes used for electrolyte supported solid oxide fuel cells, J. Power Sources 273 (2015) 237–243, https://doi.org/10.1016/j.jpowsour.2014.09.068.

[11] F. Fleischhauer, M. Terner, R. Bermejo, R. Danzer, A. Mai, T. Graule, J. Kuebler, Fracture toughness and strength distribution at room temperature of zirconia tapes used for electrolyte supported solid oxide fuel cells, J. Power Sources 275 (2015) 217–226, https://doi.org/10.1016/j.jpowsour.2014.10.083.

[12] J. Malzbender, R.W. Steinbrech, Fracture test of thin sheet electrolytes for solid oxide fuel cells, J. Eur. Ceram. Soc. 27 (7) (2007) 2597–2603, https://doi.org/10.1016/j.jeurceramsoc.2006.11.071.

[13] M. Riegraf, I. Bombarda, F. Dömling, T. Liensdorf, C. Sitzmann, N. Langhof, S. Schafföner, F. Han, N. Sata, C. Geipel, C. Walter, R. Costa, Enhancing the mechanical strength of electrolyte-supported solid oxide cells with thin and dense doped-ceria interlayers, ACS Appl. Mater. Interfaces 13 (42) (2021) 49879–49889, https://doi.org/10.1021/acsami.1c13899.

[14] A. Faes, H.L. Frandsen, A. Kaiser, M. Pihlatie, Strength of anode supported solid oxide fuel cells, Fuel Cells 11 (5) (2011) 682–689, https://doi.org/10.1002/fuce.201100038.

[15] A. Faes, H.L. Frandsen, M. Pihlatie, A. Kaiser, D.R. Goldstein, Curvature and strength of Ni-YSZ solid oxide half-cells after redox treatments, J. Fuel Cell Sci. Technol. 7 (5) (2010) 051011, https://doi.org/10.1115/1.4001019.

[16] A. Masini, T. Strohbach, F. Šiška, Z. Chlup, I. Dlouhý, Electrolyte-supported fuel cell: co-sintering effects of layer deposition on biaxial strength, Materials 12 (2) (2019) 306, https://doi.org/10.3390/ma12020306.

[17] F. Fleischhauer, R. Bermejo, R. Danzer, A. Mai, T. Graule, J. Kuebler, Strength of an electrolyte supported solid oxide fuel cell, J. Power Sources 297 (2015) 158–167, https://doi.org/10.1016/j.jpowsour.2015.07.075.

[18] P. Khajavi, J. Chevalier, P.V. Hendriksen, J.W. Tavacoli, L. Gremillard, H. L. Frandsen, Strength and hydrothermal stability of NiO–stabilized zirconia solid oxide fuel cells electrode supports, J. Eur. Ceram. Soc. 40 (8) (2021) 4206–4216, https://doi.org/10.1016/j.jeurceramsoc.2021.01.052.

[19] I. Bombarda, C. Sitzmann, T. Liensdorf, N. Langhof, S. Schafföner, Tensile testing of yittria-stabilized zirconia ceramic tapes for solid oxide cells, Int. J. Hydrogen Energy 50 (2024) 492–500, https://doi.org/10.1016/j.ijhydene.2023.08.258.

[20] C.K. Lin, J.Y. Chen, J.W. Tian, L.K. Chiang, S.H. Wu, Joint strength of a solid oxide fuel cell glass–ceramic sealant with metallic interconnect, J. Power Sources 205 (2012) 307–317, https://doi.org/10.1016/j.jpowsour.2012.01.048.

[21] C.K. Lin, Y.A. Liu, S.H. Wu, C.K. Liu, R.Y. Lee, Joint strength of a solid oxide fuel cell glass–ceramic sealant with metallic interconnect in a reducing environment, J. Power Sources 280 (2015) 272–288, https://doi.org/10.1016/j.jpowsour.2015.01.126.

[22] C.K. Lin, K.Y. Chen, S.H. Wu, W.H. Shiu, C.K. Liu, R.Y. Lee, Mechanical durability of solid oxide fuel cell glass-ceramic sealant/steel interconnect joint under thermo-mechanical cycling, Renew. Energy 138 (2019) 1205–1213, https://doi.org/10.1016/j.renene.2019.02.041.

[23] S. Celik, Influential parameters and performance of a glass-ceramic sealant for solid oxide fuel cells, Ceram. Int. 41 (2) (2015) 2744–2751, https://doi.org/10.1016/j.ceramint.2014.10.089.

[24] H. Abdoli, P. Alizadeh, D. Boccaccini, K. Agersted, Effects of thermal aging on thermo-mechanical behavior of a glass sealant for solid oxide cell applications, J. Eur. Ceram. Soc. 34 (10) (2014) 2525–2534, https://doi.org/10.1016/j.jeurceramsoc.2014.02.004.

[25] I. Ritucci, R. Kiebach, B. Talic, L. Han, P. Zielke, P. Hendriksen, H. Frandsen, Improving the interface adherence at sealings in solid oxide cell stacks, J. Mater. Res. 34 (7) (2019) 1167–1178, https://doi.org/10.1557/jmr.2018.459.

[26] L. Han, B. Talic, K. Kwok, P. Hendriksen, H. Frandsen, Interface fracture energy of contact layers in a solid oxide cell stack, ACS Appl. Energy Mater. 3 (3) (2020) 2372–2385, https://doi.org/10.1021/acsaem.9b02026.

[27] D.N. Boccaccini, O. Sevecek, H.L. Frandsen, I. Dlouhy, S. Molin, B. Charlas, J. Hjelm, M. Cannio, P.V. Hendriksen, Determination of the bonding strength in solid oxide fuel cells' interfaces by schwickerath crack initiation test, J. Eur. Ceram. Soc. 37 (2017) 3565–3578, https://doi.org/10.1016/j.jeurceramsoc.2017.04.018.

[28] Z. Xiang, W. Fenghui, H. Jianye, L. Tiejun, Determining the mechanical properties of solid oxide fuel cell by an improved work of indentation approach, J. Power Sources 201 (2012) 231–235, https://doi.org/10.1016/j.jpowsour.2011.10.125.

[29] T. Dey, A. Dey, P. Ghosh, M. Bose, A. Mukhopadhyay, R. Basu, Influence of microstructure on nano-mechanical properties of single planar solid oxide fuel cell in pre- and post-reduced conditions, Mater. Des. 53 (2014) 182–191, https://doi.org/10.1016/j.matdes.2013.06.052.

[30] M. Morales, J.J. Roa, X.G. Capdevila, M. Segarra, S. Pinol, Mechanical properties at the nanometer scale of GDC and YSZ used, Acta Mater. 58 (2010) 2504–2509, https://doi.org/10.1016/j.actamat.2009.12.036.

[31] B. Song, E. Ruiz-Trejo, A. Bertei, N.P. Brandon, Quantification of the degradation of Ni-YSZ anodes upon redox cycling, J. Power Sources 374 (2018) 61–68, https://doi.org/10.1016/j.jpowsour.2017.11.024.

[32] Z. Chen, X. Wang, V. Bhakhri, F. Giuliani, A. Atkinson, Nano-indentation of porous bulk and thin films of La$_{0.6}$Sr$_{0.4}$Co$_{0.2}$Fe$_{0.8}$O$_{3-\delta}$, Acta Mater. 61 (15) (2013) 5720–5734, https://doi.org/10.1016/j.actamat.2013.06.016.

[33] Z. Chen, X. Wang, F. Giuliani, A. Atkinson, Fracture toughness of porous material of LSCF in bulk and film forms, J. Am. Ceram. Soc. (2015) 1–8, https://doi.org/10.1111/jace.13507.

[34] Z. Chen, X. Wang, A. Atkinson, N. Brandon, Spherical indentation of porous ceramics: elasticity and hardness, J. Eur. Ceram. Soc. 36 (2016) 1435–1445, https://doi.org/10.1016/j.jeurceramsoc.2015.12.049.

[35] J. Sar, A. Almeida, R. Ghisleni, L. Dessemond, E. Djurado, Mechanical behavior of Ce$_{0.9}$Gd$_{0.1}$O$_{1.95}$-La$_{0.6}$Sr$_{0.4}$Co$_{0.2}$Fe$_{0.8}$O$_{3-\delta}$ oxygen electrode with a coral microstructure for solid oxide fuel cell and solid oxide electrolyzer cell, Ceram. Int. 42 (2016) 16981–16991, https://doi.org/10.1016/j.ceramint.2016.07.204.

[36] X.D. Wang, W.B. Guan, R. Yu, W. Liu, W.L. Pei, X.D. Zhou, Correlation of ohmic resistance and interfacial adhesion strength between cathode and electrolyte for solid oxide fuel cells, Int. J. Hydrogen Energy 41 (47) (2016) 22337–22343, https://doi.org/10.1016/j.ijhydene.2016.08.031.

[37] N. Huang, B. Han, Y. Wang, Y. Li, Y. Su, W. Guan, X. Zhou, M. Chai, S.C. Singhal, On the dependence of interfacial resistance on contact materials between cathode and interconnect in solid oxide fuel cells, Int. J. Hydrogen Energy 46 (38) (2021) 20078–20086, https://doi.org/10.1016/j.ijhydene.2021.03.128.

[38] H.S. Yoo, S.J. Kim, Y.T. Megra, J. Lee, J.W. Suk, W. Lee, Interface engineering to improve electrochemical performance of intermediate-temperature solid oxide fuel cells, Appl. Surf. Sci. 639 (2023) 158188, https://doi.org/10.1016/j.apsusc.2023.158188.

[39] J. Malzbender, R.W. Steinbrech, L. Singheiser, Determination of the interfacial fracture energies of cathodes and glass ceramic sealants in a planar solid-oxide fuel cell design, J. Mater. Res. 18 (4) (2003) 929–934, https://doi.org/10.1557/JMR.2003.0127.

[40] G. Delette, J. Laurencin, M. Dupeux, J.B. Doye, Measurement of the fracture energy at the interface between porous cathode layer and electrolyte in planar solid oxide fuel cells, Scr. Mater. 59 (2008) 31–34, https://doi.org/10.1016/j.scriptamat.2008.02.018.

[41] Y. Xie, X. Zhang, M. Robertson, R. Maric, D. Ghosh, Measurement of the interface adhesion of solid oxide fuel cells by indentation, J. Power Sources 162 (2006) 436–443, https://doi.org/10.1016/j.jpowsour.2006.07.034.

[42] J. Smolik, K. Zdunek, B. Larisch, Investigation of adhesion between component layers of a multi-layer coating TiC/Ti(C$_x$, N$_{1-x}$)/TiN by the scratch-test method, Vacuum 55 (1999) 45–50, https://doi.org/10.1016/S0042-207X(99)00122-0.

[43] L. He, Z. Xu, X. Cao, X. Zhong, R. Mu, S. He, Adhesive strength of new thermal barrier coatings of rare earth zirconates, Vacuum 83 (11) (2009) 1388–1392, https://doi.org/10.1016/j.vacuum.2009.04.053.

[44] C. Botero, L. Cabezas, V. Sarin, L. Llanes, E. Jiménez-Piqué, Nanoscratch testing of 3Al$_2$O$_3$·2SiO$_2$ EBCs: assessment of induced damage and estimation of adhesion strength, Ceramics 6 (2023) 664–677, https://doi.org/10.3390/ceramics6010040.

[45] J. Chen, S.J. Bull, Assessment of the toughness of thin coatings using nanoindentation under displacement control, Thin Solid Films 494 (1–2) (2006) 1–7, https://doi.org/10.1016/j.tsf.2005.08.176.

[46] G. Ben Ghorbal, A. Tricoteaux, A. Thuault, H. Ageorges, F. Roudet, D. Chicot, Mechanical properties of thermally sprayed porous alumina coating by Vickers and Knoop indentation, Ceram. Int. 46 (12) (2020) 19843–19851, https://doi.org/10.1016/j.ceramint.2020.05.039.

[47] N. Panic, Y. Sun, Effect of penetration depth on indentation response of soft coatings on hard substrates: a finite element analysis, Surf. Coating. Technol. 182 (2–3) (2004) 342–350, https://doi.org/10.1016/j.surfcoat.2003.07.002.

[48] I. Manika, J. Maniks, Effect of substrate hardness and film structure on indentation depth criteria for film hardness testing, J. Phys. Appl. Phys. 41 (7) (2008) 074010, https://doi.org/10.1088/0022-3727/41/7/074010.

[49] W.C. Oliver, G.M. Pharr, An improved technique for determining hardness and elastic modulus using load and displacement sensing indentation experiments, J. Mater. Res. 7 (6) (1992) 1564–1583, https://doi.org/10.1557/JMR.1992.1564.

[50] H.Y. Zhang, X.Y. Li, X.G. Wang, Nanomechanical properties of polyaniline and azo polyelectrolyte multilayer films, Chin. J. Polym. Sci. 28 (2) (2010) 269–275, https://doi.org/10.1007/s10118-010-9066-1.

[51] A. Masini, F. Šiška, O. Ševeček, Z. Chlup, I. Dlouhy, Elastic properties of multi-layered ceramic systems for SOCs, Int. J. Appl. Ceram. Technol. 15 (2) (2018) 370–379, https://doi.org/10.1111/ijac.12801.

[52] A. Nakajo, J. Kuebler, A. Faes, U.F. Vogt, H.J. Schindler, L. Chiang, S. Modena, J. V. Herle, T. Hocker, Compilation of mechanical properties for the structural analysis of solid oxide fuel cell stacks. Constitutive materials of anode-supported cells, Ceram. Int. 38 (2012) 3907–3927, https://doi.org/10.1016/j.ceramint.2012.01.043.

[53] J. Luo, R. Stevens, Porosity-dependence of elastic moduli and hardness of 3Y-TZP ceramics, Ceramics International 25 (3) (1999) 281–286, https://doi.org/10.1016/S0272-8842(98)00037-6.

[54] B. Ollivier, A. Matthews, Adhesion of diamond-like carbon films on polymers: an assessment of the validity of the scratch test technique applied to flexible substrates, J. Adhes. Sci. Technol. 8 (1994) 651–662, https://doi.org/10.1163/156856194X00401.

[55] Y.A. Farzin, M. Harenbrock, D. Nardini, A. Weber, Enhancing LSCF-based air electrode durability: insights into sulfur poisoning and air purification, Solid State Ionics 411 (2024) 116569, https://doi.org/10.1016/j.ssi.2024.116569.

[56] A. Zekri, K. Herbrig, M. Knipper, J. Parisi, T. Plaggenborg, Nickel depletion and agglomeration in SOFC anodes during long-term operation, Fuel Cells 17 (3) (2017) 359–366, https://doi.org/10.1002/fuce.201600220.

[57] Y. Zheng, Q. Li, T. Chen, W. Wu, C. Xu, W.G. Wang, Comparison of performance and degradation of large-scale solid oxide electrolysis cells in stack with different composite air electrodes, Int. J. Hydrogen Energy 40 (6) (2015) 2460–2472, https://doi.org/10.1016/j.ijhydene.2014.12.101.

[58] M. Riegraf, A. Surrey, R. Costa, Ni/CGO-based electrolyte-supported cells during Co-electrolysis: the role of feed gas impurities, ECS Trans. 103 (1) (2021) 1129, https://doi.org/10.1149/10301.1129ecst.

[59] M. Kusnezoff, N. Trofimenko, M. Müller, A. Michaelis, Influence of electrode design and contacting layers on performance of electrolyte supported SOFC/SOEC single cells, Materials 9 (11) (2016) 906, https://doi.org/10.3390/ma9110906.

[60] B.S. Prakash, R. Pavitra, S.S. Kumar, S.T. Aruna, Evaluation of solution combustion synthesized NiO/GDC ceramic powders for anode substrate and anode functional layers of intermediate temperature solid oxide fuel cell, Ceram. Int. 43 (15) (2017) 12138–12144, https://doi.org/10.1016/j.ceramint.2017.06.071.

[61] X. Lu, T.M. Heenan, J.J. Bailey, T. Li, K. Li, D.J. Brett, P.R. Shearing, Correlation between triple phase boundary and the microstructure of solid oxide fuel cell anodes: the role of composition, porosity and Ni densification, J. Power Sources 365 (2017) 210–219, https://doi.org/10.1016/j.jpowsour.2017.08.095.

[62] I. Fasaki, A. Koutoulaki, M. Kompitsas, C. Charitidis, Structural, electrical and mechanical properties of NiO thin films grown by pulsed laser deposition, Appl. Surf. Sci. 257 (2) (2010) 429–433, https://doi.org/10.1016/j.apsusc.2010.07.006.

[63] G. Abarzúa, S. Roa, N. Julve-Pérez, R.V. Mangalaraja, Solution combustion-based synthesis of NiO-GDC and NiO-SDC nanocomposites for low-temperature SOFC, Ceram. Int. 50 (9) (2024) 16689–16697, https://doi.org/10.1016/j.ceramint.2024.02.087.

[64] N. Li, A. Verma, P. Singh, J.H. Kim, Characterization of $La_{0.58}Sr_{0.4}Co_{0.2}Fe_{0.8}O_{3-\delta}$–$Ce_{0.8}Gd_{0.2}O_2$ composite cathode for intermediate temperature solid oxide fuel cells, Ceram. Int. 39 (1) (2013) 529–538, https://doi.org/10.1016/j.ceramint.2012.06.059.

[65] K. Raju, S. Kim, C.J. Hyung, J.H. Yu, Y.H. Seong, S.H. Kim, I.S. Han, Optimal sintering temperature for $Ce_{0.9}Gd_{0.1}O_{2-\delta}$–$La_{0.6}Sr_{0.4}Co_{0.2}Fe_{0.8}O_{3-\delta}$ composites evaluated through their microstructural, mechanical and elastic properties, Ceram. Int. 45 (1) (2019) 1460–1463, https://doi.org/10.1016/j.ceramint.2018.10.011.

[66] E.S. Puchi-Cabrera, M.H. Staia, A. Iost, Modeling the composite hardness of multilayer coated systems, Thin Solid Films 578 (2015) 53–62, https://doi.org/10.1016/j.tsf.2015.01.070.

[67] A.A. Griffith, VI. The phenomena of rupture and flow in solids, in: Philosophical Transactions of the Royal Society of London. Series A, Containing Papers of a Mathematical or Physical Character 582-593, 221st ed., 1921, pp. 180–183, https://doi.org/10.1098/rsta.1921.0006.

[68] R.G. Hutchinson, J.W. Hutchinson, Lifetime assessment for thermal barrier coatings: tests for measuring mixed mode delamination toughness, J. Am. Ceram. Soc. 94 (S1) (2011) S85–S95, https://doi.org/10.1111/j.1551-2916.2011.04499.x.

[69] B.U. Manam, N. Langhof, C. Sitzmann, S. Schafföner, Overview of interfacial fracture toughness testing of ceramic coatings at room and elevated temperatures, Theor. Appl. Fract. Mech. 140 (2025) 105142, https://doi.org/10.1016/j.tafmec.2025.105142.

[70] W. Li, A. Ghazanfari, D. McMillen, M. Leu, G. Hilmas, J. Watts, Properties of partially stabilized zirconia components fabricated by the ceramic on-demand extrusion process, in: Solid Freeform Fabrication 2016: Proceedings of the 27th Annual International Solid Freeform Fabrication Symposium–An Additive Manufacturing Conference, 2016, pp. 916–928.

[71] Y.J. Jang, J.I. Kim, W. Lee, J. Kim, Tribological properties of multilayer tetrahedral amorphous carbon coatings deposited by filtered cathodic vacuum arc deposition, Friction 9 (2021) 1292–1302, https://doi.org/10.1007/s40544-020-0476-y.

[72] C.L. Tien, C.Y. Chiang, C.C. Wang, S.C. Lin, Temperature-dependent residual stresses and thermal expansion coefficient of VO_2 thin films, Inventions 9 (3) (2024) 61, https://doi.org/10.3390/inventions9030061.

[73] I. Yasuda, M. Hishinuma, Lattice expansion of acceptor-doped lanthanum chromites under high-temperature reducing atmospheres, Electrochemistry 68 (6) (2000) 526–530, https://doi.org/10.5796/electrochemistry.68.526.

[74] Y.S. Touloukian, R.K. Kirby, R.E. Taylor, P.D. Desai, Thermophysical properties of matter, 13, in: Thermal Expansion: Nonmetallic Solids, Plenum Press, NY, 1977.

[75] V. Gil, J. Tartaj, C. Moure, Chemical and thermomechanical compatibility between Ni–GDC anode and electrolytes based on ceria, Ceram. Int. 35 (2009) 839–846, https://doi.org/10.1016/j.ceramint.2008.03.004.

[76] J. Xie, W. Hao, F. Wang, Parametric study on interfacial crack propagation in solid oxide fuel cell based on electrode material, Int. J. Hydrogen Energy 47 (12) (2022) 7975–7989, https://doi.org/10.1016/j.ijhydene.2021.12.153.